J. metamorphic Geol., 2012, **30**, 413–434 doi:10.1111/j.1525-1314.2012.00973.x

The thermal structure of continental crust in active orogens: insight from Miocene eclogite and granulite xenoliths of the Pamir Mountains

S. M. GORDON,[1]* P. LUFFI,[2] B. HACKER,[1] J. VALLEY,[3] M. SPICUZZA,[3] R. KOZDON,[3] P. KELEMEN,[4] L. RATSHBACHER[5] AND V. MINAEV[6]
[1]*Earth Research Institute, University of California, Santa Barbara, CA 93106, USA (staciag@unr.edu)*
[2]*Department of Earth Science, Rice University, Houston, TX 77005, USA*
[3]*WiscSIMS, Department of Geoscience, University of Wisconsin, Madison, WI 53706, USA*
[4]*Lamont-Doherty Earth Observatory, Columbia University, Palisades, NY 10964, USA*
[5]*Geowissenschaften, Technische Universität Bergakademie Freiberg, D-09599 Freiberg, Germany*
[6]*Tajik Academy of Sciences, 734063 Dushanbe, Tajikistan*

ABSTRACT Rare ultrahigh-temperature–(near)ultrahigh-pressure (UHT–near-UHP) crustal xenoliths erupted at 11 Ma in the Pamir Mountains, southeastern Tajikistan, preserve a compositional and thermal record at mantle depths of crustal material subducted beneath the largest collisional orogen on Earth. A combination of oxygen-isotope thermometry, major-element thermobarometry and pseudosection analysis reveals that, prior to eruption, the xenoliths partially equilibrated at conditions ranging from 815 °C at 19 kbar to 1100 °C at 27 kbar for eclogites and granulites, and 884 °C at 20 kbar to 1012 °C at 33 kbar for garnet–phlogopite websterites. To reach these conditions, the eclogites and granulites must have undergone mica-dehydration melting. The extraction depths exceed the present-day Pamir Moho at ~65 km depth and suggest an average thermal gradient of ~12–13 °C km^{-1}. The relatively cold geotherm implies the introduction of these rocks to mantle depths by subduction or gravitational foundering (transient crustal drip). The xenoliths provide a window into a part of the orogenic history in which crustal material reached UHT–(U)HP conditions, partially melted, and then decompressed, without being overprinted by the later post-thermal relaxation history.

Key words: garnet–omphacite xenoliths; granulite xenoliths; oxygen isotopes; Pamir; partial melting.

INTRODUCTION

The thermal structure of collisional orogenic belts depends on a variety of factors including the rate of subduction, accretion and denudation, the radiogenic heat production, thermal conductivity and the rheology of the underlying lithospheric mantle (e.g. Royden, 1993; Peacock, 1995; Huerta *et al.*, 1998; Pope & Willett, 1998). As most of these factors evolve over the course of orogenesis, the thermal structure changes as the lithosphere thickens, undergoes thermal relaxation and collapses. Therefore, understanding the thermal structure is important for predicting the overall rheological behaviour of collisional orogenic belts (e.g. is partial melting possible? England & Thompson, 1984; Patiño Douce & McCarthy, 1998; Hacker *et al.*, 2000; Erkan & Blackwell, 2008). However, access to rocks from different parts of thickened crust within collisional orogenic belts and to different stages of the thermal evolution (e.g. shortening, thermal relaxation, and collapse) is generally limited.

A suite of Miocene xenoliths erupted in the Pamir Mountains of Tajikistan consists of eclogites and granulites with bulk compositions that suggest that the xenoliths have crustal protoliths (Fig. 1; Dmitriev, 1976; Ducea *et al.*, 2003; Hacker *et al.*, 2005). Some of the eclogite xenoliths equilibrated at 25–28 kbar and 1000–1100 °C (Hacker *et al.*, 2005), just below the coesite-stability field. A group of plagioclase-bearing granulite xenoliths, not studied by Hacker *et al.* (2005), probably equilibrated at lower pressure. All xenoliths were erupted at the same time (11.5 ± 0.2 Ma, ^{40}Ar–^{39}Ar; Hacker *et al.*, 2005) and thus provide insight into the evolving thermal structure of the largest collisional belt in the world, the Pamir Mountains–Tibet system.

To understand the transient thermal structure of orogenic systems, the *P–T–t* path that the rocks experienced must be determined. Because UHP rocks represent the deepest exposed portions of orogenic belts, numerous studies have focused on determining the peak pressures and temperatures achieved by these rare rocks (e.g. Nakamura & Banno, 1997; Ravna, 2000; Krogh Ravna & Terry, 2004; Nakamura & Hirajima, 2005; Hacker, 2006; Ernst *et al.*, 2007). Most temperature estimates of eclogites have relied on Fe–Mg equilibrium between garnet and clinopyroxene. The accuracy of this thermometer is affected, however, by the Fe^{3+}/Fe^{2+} ratios, which are typically not measured (e.g. Krogh Ravna & Paquin, 2003;

---

* *Present address*: Department of Geological Sciences, University of Nevada, Reno, NV 89557, USA

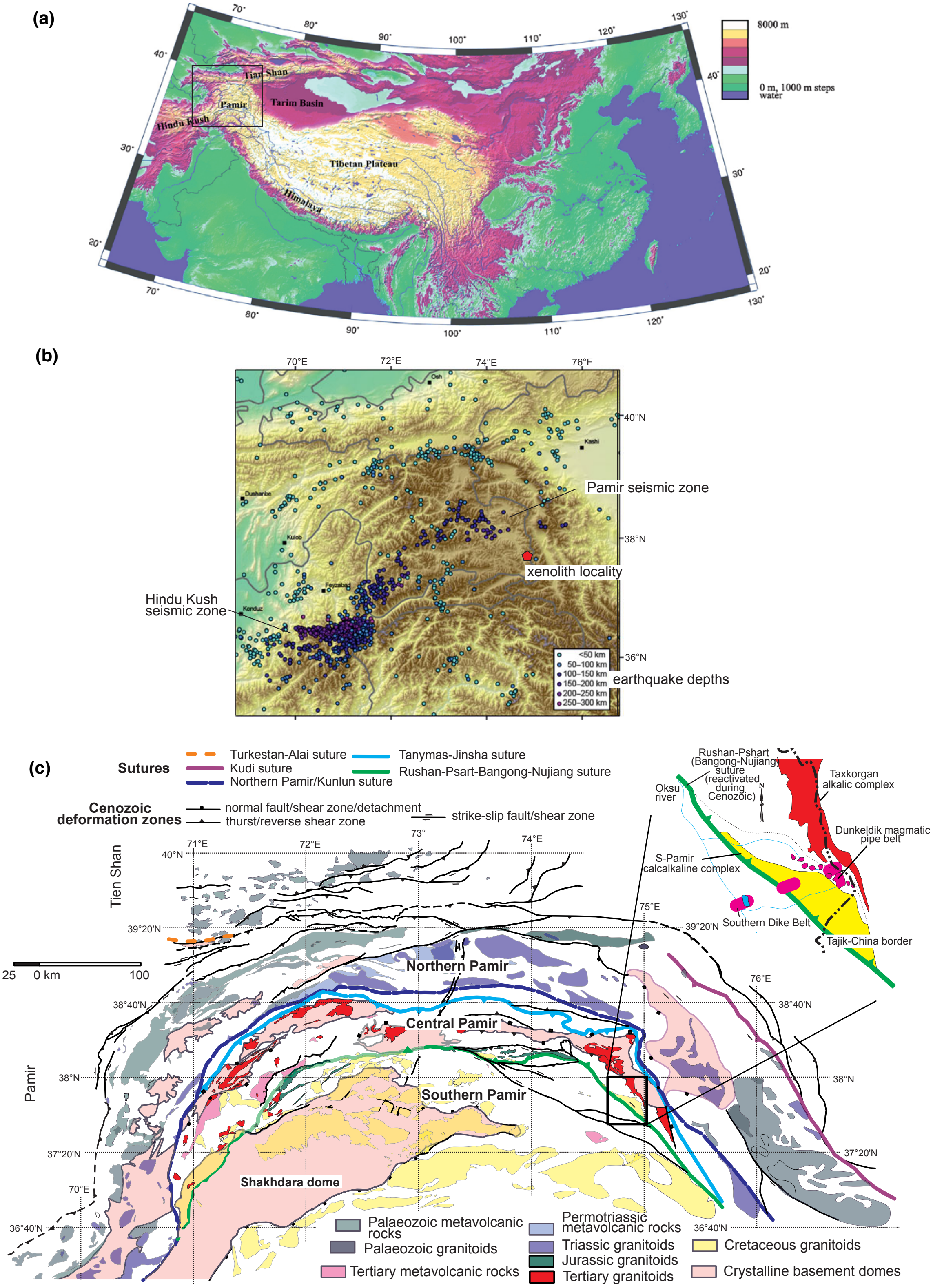

Fig. 1. (a) Digital elevation map of the Pamir Mountains–Tibet–Himalayan system; (b) southeastern Pamir xenolith locality plotted in relation to the Pamir Mountains and Hindu-Kush seismic zones; seismicity from Engdahl *et al.* (1998); (c) simplified geological and structural map of the Pamir Mountains and northern Karakoram, showing Palaeozoic to Tertiary magmatic belts and sutures, Cenozoic gneiss domes, major Cenozoic faults and the location of the Dunkeldik magmatic field (marked by box) (strongly modified from Vlasov *et al.*, 1991; Schwab *et al.*, 2004; Hacker *et al.*, 2005).

Proyer *et al.*, 2004; Stípská & Powell, 2005). Oxygen-isotope thermometry represents a complementary method and a check for major-element thermometry. For the Pamir Mountains xenoliths, oxygen diffusion should have been negligible during the rapid eruption and cooling experienced by these xenoliths (Hacker *et al.*, 2005), and therefore, fractionation of oxygen isotopes among the minerals should reflect pre-eruption metamorphic equilibrium (e.g. Sharp *et al.*, 1992, 1993; Rumble & Yui, 1998; Zheng *et al.*, 1998; Valley, 2001; Schulze *et al.*, 2003a). In addition, some complications associated with major-element thermobarometry, such as non-ideal mixing, H_2O activity and pressure dependence, do not affect oxygen-isotope fractionation (Hoering, 1961; Wolfsberg, 1972; Clayton *et al.*, 1975). A combination of conventional thermobarometry and oxygen thermometry techniques can be applied to the Pamir Mountains xenoliths to assess mineral equilibrium and pre-eruption *P–T* conditions, which were reached during crustal thickening of a large orogen.

In this study, phase equilibria and pre-eruption *P–T* conditions are estimated from eclogite and granulite xenoliths by combining oxygen-isotope thermometry, major-element thermobarometry and pseudosections. The samples represent a range of protoliths, from gabbro–granodiorite (for the eclogites) to peraluminous metasedimentary rocks (for the granulites). To further constrain the thermal structure of the region, we also discuss the *P–T* equilibration of several websterite xenoliths. It is found that at depths of ~60–100 km, the Miocene crust of the Pamir Mountains consisted of eclogite interlayered with garnet–kyanite granulites and websterites. The xenoliths record probable subduction of crustal material in an actively shortening collisional orogen. The granulite xenoliths suggest some cooling and decompression prior to the final eruption at 11 Ma (Hacker *et al.*, 2005).

GEOLOGICAL SETTING

The Pamir Mountains represent the westernmost extent of the Pamir Mountains–Tibet orogen (Fig. 1a). Similar to Tibet, the Pamir Mountains constitute a plateau with a thick crust (~65 km; Beloussov *et al.*, 1980; Mechie *et al.*, 2011), resulting from 1800–2100 km of Cenozoic intracontinental shortening (Johnson, 2002) associated with the India–Eurasia collision. However, in comparison to Tibet, the shortening has been accommodated in half the orogenic width. The Pamir Mountains are still shortening at a rate of 16–20 mm yr^{-1} (Reigber *et al.*, 2001; Mohadjer *et al.*, 2010) and are underlain by intermediate-depth seismicity that may be associated with intracontinental subduction (Fig. 1b; e.g. Pegler & Das, 1998; Negredo *et al.*, 2007). Three belts of mid- to lower-crustal gneiss domes were exhumed chiefly between 25 and 10 Ma (Fig. 1c, Robinson *et al.*, 2007; McGraw *et al.*, 2010; Stearns *et al.*, 2011). A variety of Cretaceous granitoids to Miocene shoshonitic/calcalkaline igneous bodies intruded the Pamir Mountains crust, including the domes (Schwab *et al.*, 2004).

The volcanic pipes that host the xenoliths studied in this article (first described by Dmitriev, 1976) belong to the Dunkeldik magmatic field in the southeastern Pamir (Fig. 1c). The Dunkeldik magmatic field is the result of the youngest known magmatism in the Pamir Mountains (*c.* 11 Ma; Hacker *et al.*, 2005) and consists of ultrapotassic (4–7 wt% K_2O; K_2O/Na_2O = 4–7) dykes, pipes and sub-volcanic bodies that range from alkali basalt, to trachyte, syenite and carbonatite (Dmitriev, 1976). The field is exposed between the Late Triassic–Early Jurassic Tanymas suture and the Late Jurassic–Early Cretaceous Rushan–Pshart suture, in an area of active deformation related to the Karakoram fault zone (Fig. 1c; Dmitriev, 1976; Strecker *et al.*, 1995). The Dunkeldik xenolith suite consists of 38% eclogite and garnet–omphacite granulite, 19% phlogopite pyroxenite and glimmerite, 15% biotite–garnet clinopyroxenite, 8% garnet–biotite gneiss, 6% garnet–kyanite granulite, 4% garnet gneiss, 3% phlogopite–garnet websterite and 7% other rocks (Lutkov, 2003). The xenoliths are up to 50 cm in diameter and most are foliated. Hacker *et al.* (2005) studied six of these xenoliths, including sanidine ± biotite eclogite, felsic garnet–sanidine–kyanite ± biotite granulites and glimmerite. Major-element thermobarometry revealed equilibration of the eclogites at 1000–1100 °C and 25–28 kbar. The rocks were interpreted to be residues of high-pressure dehydration melting and K-rich metasomatism of granodioritic to gabbroic protoliths. Our study not only focuses on seven garnet–kyanite granulites, but also includes one garnet–omphacite granulite, two eclogites, one garnet–biotite gneiss and five websterites; these rocks equilibrated at a broader range of pressures and temperatures and, thus, provide more constraints on the thermal structure of the Miocene Pamir crust. Analytical methods are outlined in Appendices S1 and S2.

RESULTS

Mineral chemistry and bulk-rock compositions

The studied xenoliths form a continuous compositional series, from quartzofeldspathic garnet–kyanite granulites to eclogite (Table 1). Their protoliths were likely magmatic (i.e. granodioritic–gabbroic) and metasedimentary rocks. Mineral compositions for all samples are reported in Table S1.

Garnet–biotite gneiss

Garnet–biotite gneiss DK83 has a grano-lepidoblastic texture, with 22 vol.% biotite that defines a strong foliation along with quartz and feldspar (Fig. 2a). Grain sizes average 0.5–1.0 mm. The matrix biotite is Ti rich (TiO_2 = 7.1 wt%), whereas biotite inclusions

Table 1. Measured bulk compositions of the Pamir Mountains xenoliths.

Sample	DK7	DK13	DK32	DK43	DK63	DK69	DK71	DK74	DK83	DK84	1309
XRF											
SiO_2	69.57	59.01	50.44	69.01	49.20	63.13	57.60	60.43	62.44	48.74	56.05
TiO_2	1.22	1.26	1.63	0.77	1.19	0.69	1.13	0.80	0.66	1.16	0.90
Al_2O_3	14.42	19.95	17.40	13.43	24.66	15.08	17.42	19.63	14.72	19.65	19.12
FeO*	5.97	8.38	9.33	5.43	14.21	6.04	8.60	6.86	4.88	9.57	7.15
MnO	0.15	0.18	0.17	0.12	0.82	0.29	0.17	0.15	0.10	0.23	0.12
MgO	1.89	2.83	4.01	1.92	3.57	2.05	3.24	2.77	2.81	4.25	3.72
CaO	0.88	1.43	9.59	0.59	1.68	3.33	2.59	2.10	3.28	7.54	6.70
Na_2O	0.62	0.88	2.96	0.93	0.57	1.61	0.82	0.90	2.51	2.42	2.46
K_2O	3.89	4.04	2.03	3.77	3.87	4.75	4.86	3.89	4.21	4.18	3.80
P_2O_5	0.03	0.18	0.25	0.03	0.26	0.12	0.22	0.04	0.32	0.25	0.20
Sum	98.64	98.13	97.79	96.00	100.03	97.08	96.64	97.56	95.93	97.99	100.22

Oxides in wt%. Analyses accomplished using the XRF at Washington State University (Johnson *et al.*, 1999).

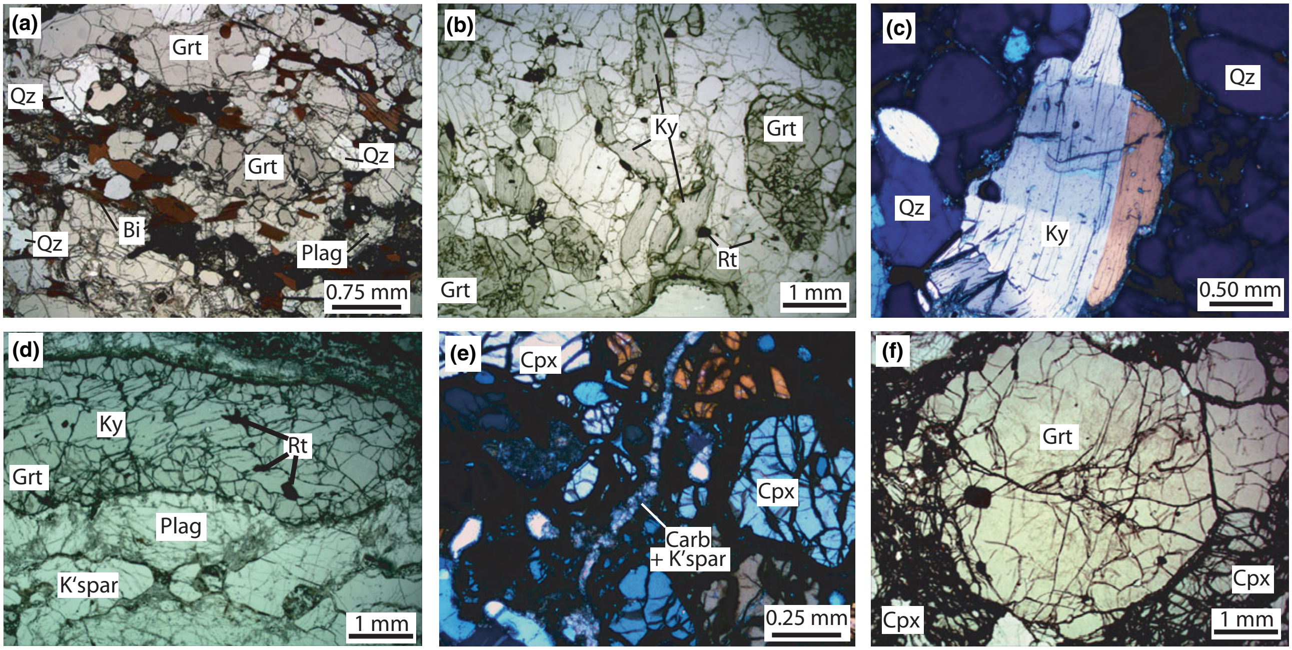

Fig. 2. Representative photomicrographs from the Pamir Mountains xenoliths: (a) garnet–biotite gneiss DK83 with lobate quartz grain boundaries; (b) kinked and tabular kyanite surrounded by feldspar and quartz in granulite DK63; (c) tabular twinned kyanite with undulatory extinction in granulite DK63; (d) garnet encloses elongate kyanite in granulite DK69, with a ribbon of sanidine also parallel to foliation; (e) carbonate and sanidine veins cut clinopyroxene in eclogite DK84; and (f) garnet rimmed mostly by altered omphacite in eclogite DK84. Carb = carbonate; Cpx = clinopyroxene; Grt = garnet; K-spar = alkali feldspar; Ky = kyanite; Qz = quartz; Plag = plagioclase Rt = rutile.

in garnet have less TiO_2 (~4.7 wt%) and higher Mg# (molar Mg/(Mg + Fe); 0.66 *v.* 0.63 for matrix biotite). The garnet (~12 vol.%) is anhedral and shows weak zoning, with $Alm_{50}Prp_{01}Grs_{38}Sps_{11}$ cores and $Alm_{53}Prp_{03}Grs_{35}Sps_{09}$ rims (Fig. 3a); these compositions are significantly different from the garnet in other xenoliths (Fig. 3a; see below). Homogeneous plagioclase ($An_{28–29}Ab_{61–62}Or_{09–10}$) and alkali feldspar ($An_{00}Ab_{02}Or_{98}$) are present throughout the matrix (Fig. 3c). Matrix quartz has lobate boundaries; some grains form ribbons or have chessboard extinction. Throughout the sample, carbonate veins parallel the foliation, and carbonate-filled cracks occur in garnet. Carbonate + K-feldspar aggregates replace an unknown mineral. Overall, the garnet–biotite gneiss represents a rare rock type within the xenolith suite; there are few xenoliths that contain hydrous minerals.

Garnet–omphacite granulite

In general, the garnet–omphacite granulite DK32 is similar in texture and composition to the eclogites and garnet–kyanite granulites (described in the next sec-

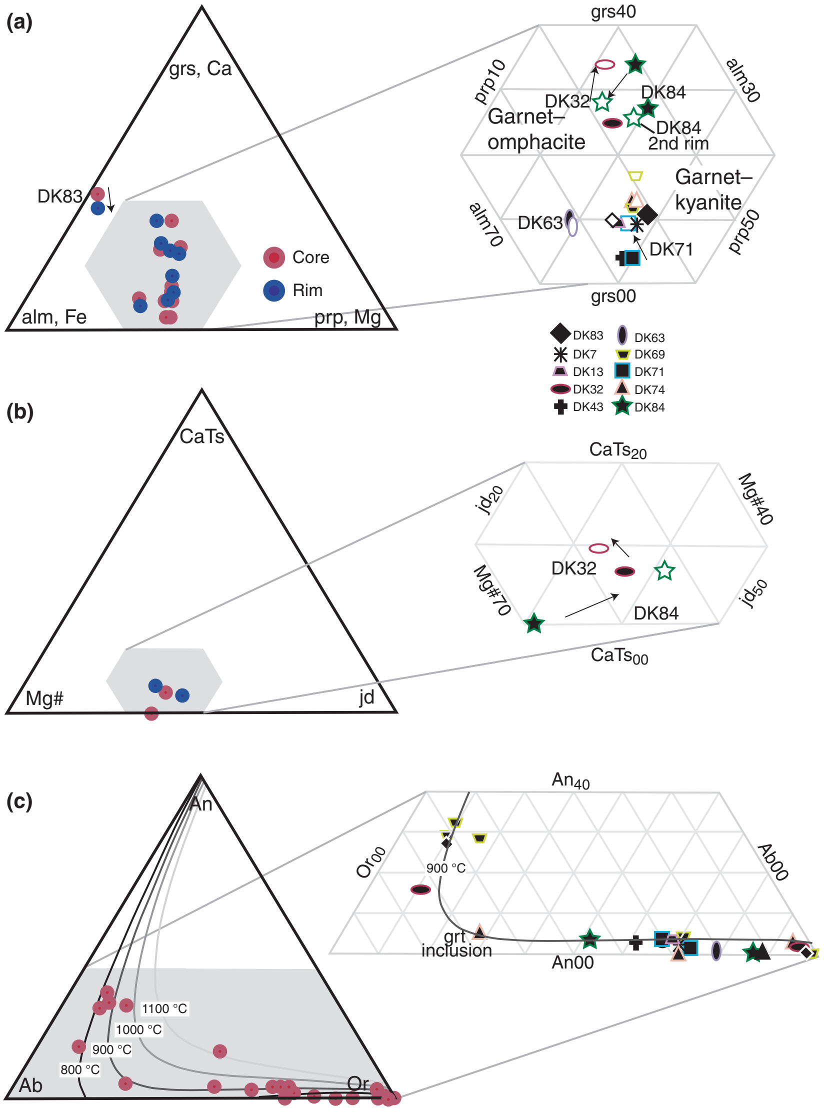

Fig. 3. (a) Grossular–almandine–pyrope compositions of garnet. Arrows show core to rim zoning; (b) Ca-Tschermak, Mg-number and acmite + jadeite components of clinopyroxene; and (c) albite–anorthite–orthoclase compositions of feldspar with solvus isotherms at 17 kbar (Elkins & Grove, 1990). For all samples, the black fill indicates the core composition, whereas the white fill indicates the rim composition.

tions) but contains plagioclase and omphacite in equilibrium with garnet, kyanite and alkali feldspar.

The grains in xenolith DK32 have an average size of 0.5–1.5 mm. Garnet cores are $Alm_{48}Prp_{26}Grs_{25}Sps_{01}$, and rims are $Alm_{44}Prp_{21}Grs_{34}Sps_{01}$ (Fig. 3a). Omphacite shows a rimward decrease in jadeite content from 37 to 33 mol.% and in Mg# from 0.67 to 0.64 in the outermost 50 μm (Fig. 3b). Micron-scale carbonate veins $(Ca_{0.58-0.60}Mg_{0.28-0.30}Fe_{0.11-0.12})CO_3$ cut the rock, and 100–500 μm calcite grains $(Ca_{0.96}Mg_{0.02}Fe_{0.02})CO_3$ are spatially associated with plagioclase and omphacite. Coronas around clinopyroxene consist of quartz, oligoclase $(An_{15}Ab_{73}Or_{12})$ and sanidine $(An_{00}Ab_{02-06}Or_{94-98})$ (Fig. 3c). Clinopyroxene in these coronas has a much lower jadeite content of 11 mol.%, and clinopyroxene in fractures that cut garnet has only 4 mol.% jadeite. Homogeneous oligoclase $(An_{16}Ab_{73}Or_{11})$ throughout the thin section appears to be in textural equilibrium with garnet and omphacite (Fig. 3c). Most quartz grains and minor, skeletal kyanite are surrounded by alkali-feldspar coronas $(An_{00-03}Ab_{02-04}Or_{93-98}$; Fig. 3c).

Garnet–kyanite granulites

In general, the garnet–kyanite granulites only show minor alteration at the tens of micron scale, mostly on the rims of garnet, including symplectite coronas composed of two feldspars $(An_{00-01}Ab_{03-04}Or_{96-99}$ and $An_{01-03}Ab_{23-31}Or_{66-75})$ ± quartz ± spinel. Veins of similar feldspars locally cut garnet and surround garnet inclusions; in the matrix, Or_{96-99} feldspar forms coronae around kyanite. The veins also contain local carbonate $(Ca_{50-59}Mg_{25-36}Fe_{12-19})$. Minor-oriented ilmenite lamellae are found in rutile. Below, each sample is described in more detail.

The plagioclase-bearing garnet–kyanite granulite DK69 contains abundant, up to ~1 cm long kyanite.

Garnet, plagioclase, minor alkali feldspar and quartz are also present and have an average grain size of 1–2 mm. Minor graphite is present in the matrix. Garnet occurs both as porphyroblasts and as coronae on kyanite (Fig. 2d); all garnet grains are zoned from $\mathrm{Alm_{50}Prp_{35}Grs_{12}Sps_{03}}$ cores to $\mathrm{Alm_{48}Prp_{32}Grs_{17}Sps_{03}}$ rims, with similar rim compositions at the kyanite interface as well as at the interface with feldspar (Fig. 3a). Homogeneous $\mathrm{An_{29–32}Ab_{58–60}Or_{09–11}}$ plagioclase dominates the matrix, whereas plagioclase included in garnet is zoned from cores of $\mathrm{An_{33–34}Ab_{57–58}Or_{08–09}}$ to rims of $\mathrm{An_{29–32}Ab_{46–55}Or_{14–25}}$ (Fig. 3c). K-feldspar inclusions in garnet have $\mathrm{An_{04}Ab_{26}Or_{70}}$ rims and $\mathrm{An_{04}Ab_{30}Or_{66}}$ cores or are homogeneous $\mathrm{Or_{99}}$. The matrix alkali feldspar ($\mathrm{An_{04–05}Ab_{28–30}Or_{65–67}}$) occurs in ribbons parallel to the elongate garnet and kyanite grains, and is associated with calcite ($\mathrm{(Ca_{0.95–0.97}Mg_{0.01}Fe_{0.01–0.04})CO_3}$ nodules, which are also present as inclusions in garnet.

Quartz, sanidine and elongate garnet define a strong foliation in DK7. The sample is porphyroblastic, with an average grain size of 1–2 mm. Garnet is up to 1 cm in diameter and homogenous ($\mathrm{Alm_{53}Prp_{37}Grs_{09}Sps_{01}}$; Fig. 3a); it contains inclusions of quartz, sanidine, kyanite and graphite. Matrix quartz displays chessboard extinction. Matrix kyanite is bent around garnet grains and is typically surrounded by a moat of alkali feldspar similar in composition to the coarser feldspar grains ($\mathrm{An_{02–03}Ab_{26–29}Or_{68–72}}$; Fig. 3c). Abundant fluid/melt inclusions in the kyanite are elongate parallel to the fold hinges in the host grain and sub-parallel to the matrix foliation. Rutile crystals are large (> 1 mm), homogeneous and xenoblastic.

Granulite DK13 has a strong foliation defined by elongate garnet, kyanite and quartz. The sample consists of ~41 vol.% garnet, ~15% quartz, ~12% kyanite and ~30% alkali feldspar ($\mathrm{An_{01–03}Ab_{26–30}Or_{68–76}}$; Fig. 3c). The grain size averages 1–2 mm. The majority of garnet show only micron-scale rim alteration and is homogeneous $\mathrm{Alm_{55}Prp_{35}Grs_{09}Sps_{01}}$ (Fig. 3a). Elongated kyanite, as well as sanidine, mica, quartz, rutile and apatite, are included in garnet. As in DK7, kyanite contains abundant fluid/melt inclusions, is bent and is rimmed by alkali feldspar of the same composition as in the matrix.

Granulite DK43 has a strong foliation defined by quartz (~63 vol.%), alkali feldspar (~17%), garnet (12%) and kyanite (~8%). The grain-size averages 1–2 mm, with coarser quartz and feldspar (~1 mm) than in other samples. Garnet forms small (2 mm), homogeneous ($\mathrm{Alm_{56}Prp_{39}Grs_{04}Sps_{01}}$), typically elongated xenoblasts (Fig. 3a), with few quartz and kyanite inclusions. The matrix alkali feldspar is homogeneous $\mathrm{An_{03}Ab_{36}Or_{61}}$ (Fig. 3c). Most kyanite grains are surrounded by moats of late feldspar ($\mathrm{Or_{97–99}}$) (Fig. 3c); some have undulatory extinction and fluid/melt(?) inclusion trails.

Granulite DK63 is characterized by ~15 vol.% deformed kyanite in up to 0.5 cm elongate crystals that define the foliation (Fig. 2b). Quartz, sanidine and garnet have an average grain size of 0.5–1.5 mm. Kyanite is commonly twinned and displays undulatory extinction (Fig. 2b,c); kyanite included in garnet is undeformed. Garnet is slightly zoned, with inclusion-rich, altered and fractured cores of $\mathrm{Alm_{59}Prp_{27}Grs_{10}Sps_{04}}$ and inclusion-free, homogeneous rims of $\mathrm{Alm_{60}Prp_{29}Grs_{08}Sps_{03}}$ (Fig. 3a). Alkali feldspar is homogeneous $\mathrm{An_{01}Ab_{21}Or_{78}}$ (Fig. 3c).

Sample DK71 contains subidioblastic garnet in a matrix of alkali feldspar (~30 vol.%), quartz (~20%) and kyanite (~8%). The feldspar and kyanite define the foliation and have an average grain size of 1–2 mm. The garnet grains are zoned in their outermost ~50 μm, from $\mathrm{Alm_{57}Prp_{38}Grs_{04}Sps_{01}}$ to $\mathrm{Alm_{53}Prp_{36}Grs_{10}Sps_{01}}$ rims (Fig. 3a). Alkali feldspar is homogeneous $\mathrm{An_{02}Ab_{26}Or_{72}}$ (Fig. 3c). Kyanite is kinked, has undulatory extinction and is typically surrounded by late $\mathrm{An_{04}Ab_{28}Or_{68}}$ feldspar. Similar coronas between kyanite and garnet contain $\mathrm{An_{15}Ab_{38}Or_{47}}$ feldspar. Quartz forms elongate ribbons that wrap around garnet.

Granulite DK74 is granoblastic, with ~1 mm grains of garnet, quartz, kyanite and alkali feldspar that define a weak foliation. Garnet is weakly zoned, from $\mathrm{Alm_{51}Prp_{35}Grs_{13}Sps_{01}}$ cores to $\mathrm{Alm_{51}Prp_{36}Grs_{12}Sps_{01}}$ rims (Fig. 3a). They are sub- to idioblastic and have ~10–20 μm rims of feldspar and carbonate ($\mathrm{Ca_{51–56}Mg_{30–34}Fe_{13–16}}$). Feldspar ($\mathrm{An_{00–03}Ab_{00–08}Or_{92–99}}$) plus carbonate coronas surround quartz and kyanite that are adjacent to garnet. The matrix feldspar is similar in composition to the corona feldspar but locally has more sodic ($\mathrm{An_{02}Ab_{16}Or_{83}}$) rims (Fig. 3c). The alkali feldspar in the matrix and in garnet strain shadows is zoned from $\mathrm{An_{00}Ab_{16}Or_{84}}$ cores to $\mathrm{An_{00}Ab_{29}Or_{71}}$ rims (Fig. 3c). Garnet contains inclusions of $\mathrm{Or_{99}}$ and $\mathrm{An_{05}Ab_{68}Or_{27}}$ alkali feldspar.

Sanidine eclogites

The garnet- and omphacite-dominated samples, including DK84 and 1309, contain kyanite, quartz, sanidine, and minor rutile, apatite, zircon and monazite. The samples are transected by small veins of feldspar or carbonate (see below; Fig. 2e). In addition, garnet and omphacite have < 10 μm thick quartz + feldspar coronas.

Eclogite DK84 (Fig. 2e,f) has a foliation defined by the shape-preferred orientation of omphacite, quartz and sanidine. The garnet grains are zoned, and different grains have distinct rim compositions. Some have $\mathrm{Alm_{40}Prp_{25}Grs_{34}Sps_{01}}$ core, a $\mathrm{Alm_{44}Prp_{31}Grs_{24}Sps_{01}}$ mantle and $\mathrm{Alm_{47}Prp_{25}Grs_{27}Sps_{01}}$ rim (Fig. 3a); others have rims of $\mathrm{Alm_{42}Prp_{22}Grs_{34}Sps_{02}}$. Most garnet has a ~50 μm corona of intermingled $\mathrm{An_{01}Ab_{12}Or_{87}}$ and $\mathrm{An_{04}Ab_{61}Or_{35}}$ feldspar (Fig. 3c). The omphacite grains have cores of 32 mol.% Jd and Mg# 0.71 and rims of 42 mol.% Jd and Mg# 0.64 (Fig. 3b). Micron-scale carbonate veins $\mathrm{(Ca_{0.52–0.62}Mg_{0.25–0.30}Fe_{0.12–0.18})CO_3}$

traverse the sample and cut garnet (Fig. 2e). Coronas (>10 μm thick) of sodic clinopyroxene + plagioclase have replaced $<10\%$ of the omphacite. Homogeneous sanidine ($An_{04–06}Ab_{43–50}Or_{44–54}$) is interspersed and in textural equilibrium with omphacite and garnet (Fig. 3b). Minor quartz ($\sim$10%) is typically associated with kyanite, but also occurs as inclusions in omphacite. Quartz–omphacite boundaries are separated by a film of quartz and feldspar ($An_{01}Ab_{03}Or_{96}$). Kyanite grains are surrounded by coronas of two feldspars, $An_{01}Ab_{25}Or_{74}$ and $An_{12}Ab_{81}Or_{07}$.

Eclogite 1309, described in Hacker *et al.* (2005), consists of garnet, omphacite, sanidine, kyanite, quartz and rutile. Garnet and clinopyroxene are homogeneous, whereas the sanidine is zoned outward from a $Or_{73–74}Ab_{25}$ core to a $Or_{56–68}Ab_{31–43}$ rim. Like DK84, veins of carbonate cut the sample.

Garnet–phlogopite websterites

The websterite xenoliths (samples 1170, DK17, DK24, DK57, DK70) are foliated and range from granoblastic to porphyroblastic and grano–lepidoblastic. The foliation is defined by the shape-preferred orientation of phlogopite and/or pyroxene. They consist mainly of orthopyroxene, clinopyroxene, garnet and phlogopite and <1 vol.% apatite and pyrrhotite or rutile. Grain sizes average 1–2 mm, but poikiloblastic garnet reaches 3–5 mm. Unlike the eclogites, the garnet in websterites shows no significant compositional variability in individual samples (Table S1); compositions range from $Prp_{55}Alm_{33}Grs_{11}Sps_{01}$ to $Prp_{35}Alm_{56}Grs_{08}Sps_{01}$. Pyroxene-dominated patches are granoblastic–polygonal, with typical 120° triple junctions. Clinopyroxene ranges from sodic augite to omphacite but is nearly homogeneous in each sample; the overall compositional range is $Di_{44–68}Hed_{12–15}Jd_{5–25}CaTs_{01–06}(En + Fs)_{08–15}$ (Table S1). Some matrix clinopyroxene is surrounded by <10 μm symplectite rims of a Na-poor clinopyroxene and ternary feldspar. Orthopyroxene grains are in general homogeneous with compositions falling in the $En_{71–78}Fs_{16–23}(Di + Hd)_{02–05}MgTs_{01–02}$ range; some larger grains display Al zoning (Table S1). Matrix orthopyroxene grains are coated by narrow selvages of unidentified, late submicroscopic minerals (likely phyllosilicate and/or amphibole). Phlogopite is in general homogeneous in composition (Table S1); in some websterites, it appears to be in textural equilibrium with other phases, whereas in other samples, it is secondary after pyroxene, indicating late potassium metasomatism. The websterites show varying degrees of alteration and local disequilibrium, which are mostly confined to the rinds of the xenoliths where late phlogopite formation and clinopyroxene breakdown to symplectite are abundant. Garnet and pyroxene away from the rinds are much less altered. The outermost mineral rims locally display distinct Mg# increases even in the cores of some of the xenoliths.

Oxygen-isotope data

Oxygen isotopes from the eight granulites and two eclogites were first measured using the laser-fluorination technique on bulk separates of kyanite, garnet, quartz and rutile to obtain high-precision measurements at the millimetre- to centimetre-scale (Fig. 4, Table 2). The $\delta^{18}O_{quartz}$ values range from 8.4‰ to 15.4‰ (Fig. 4), with the lighter values from eclogites 1309 and DK84, and garnet–omphacite granulite DK32. Garnet $\delta^{18}O$ values parallel those in quartz, and range from 6.8‰ in eclogite 1309 to 14.3‰ in garnet–kyanite granulite DK7 (Fig. 4a). Garnet in garnet–omphacite granulite DK32 is inhomogeneous, with a $\sim$0.9‰ difference between the two laser-fluorination analyses. Kyanite $\delta^{18}O$ values range from 7.7‰ to 14.4‰ (Fig. 4b). Rutile yielded the lightest $\delta^{18}O$ values 6.6–11.0‰ in DK32 and DK84, and 9.9–11.9‰ in the remaining granulites (Fig. 4c).

To determine whether the minerals are homogeneous in $\delta^{18}O$ at single grain and sample scales, *in situ* oxygen-isotope measurements on quartz, rutile, kyanite, garnet and zircon were performed by ion microprobe (Fig. 5, Tables 3 & S2). The ion-microprobe analyses targeted the extremes in major-element zoning where found in garnet; in other minerals, cores and rims were analysed. Thus, the *in situ* data are not necessarily representative of the average values measured by laser fluorination. For the ion-microprobe analyses on rutile, only the precision within grains can be compared and not from grain to grain. The instrumental mass fractionation for rutile varies according to the orientation of the crystal lattice relative to the primary and secondary beams of the ion microprobe, and it is not possible to accurately convert the raw ion-microprobe data to the VSMOW scale for this mineral. Thus, grain-to-grain rutile comparison is not possible as each grain may have a different orientation. Overall, the results for the different minerals show some zoning in the $\delta^{18}O$ of individual grains as well as grain-to-grain variability for the minerals except for rutile.

The kyanite ion-microprobe values of $\delta^{18}O$ are similar to those obtained through laser fluorination and overlap with 99% confidence (Fig. 5a). The kyanite grains reveal a spread in values (0.2–0.9‰ 2σ standard deviation) when including all of the data for the individual samples (Fig. 5a, Table S3). The spread is not caused by zoning within individual grains but rather differences from grain to grain.

The ion-microprobe results on garnet cluster near the laser data, but like kyanite, reveal heterogeneity (Fig. 5b, Table S3). As described above, most garnet is zoned in major cations; however, $\delta^{18}O$ does not typically follow the same zoning trend. In general, individual grains are homogeneous and the variability in $\delta^{18}O$ measurements reflects grain-to-grain differences. The garnet in granulite DK32 tends to have lighter rims ($\sim$12.1‰) than cores ($\sim$12.5‰).

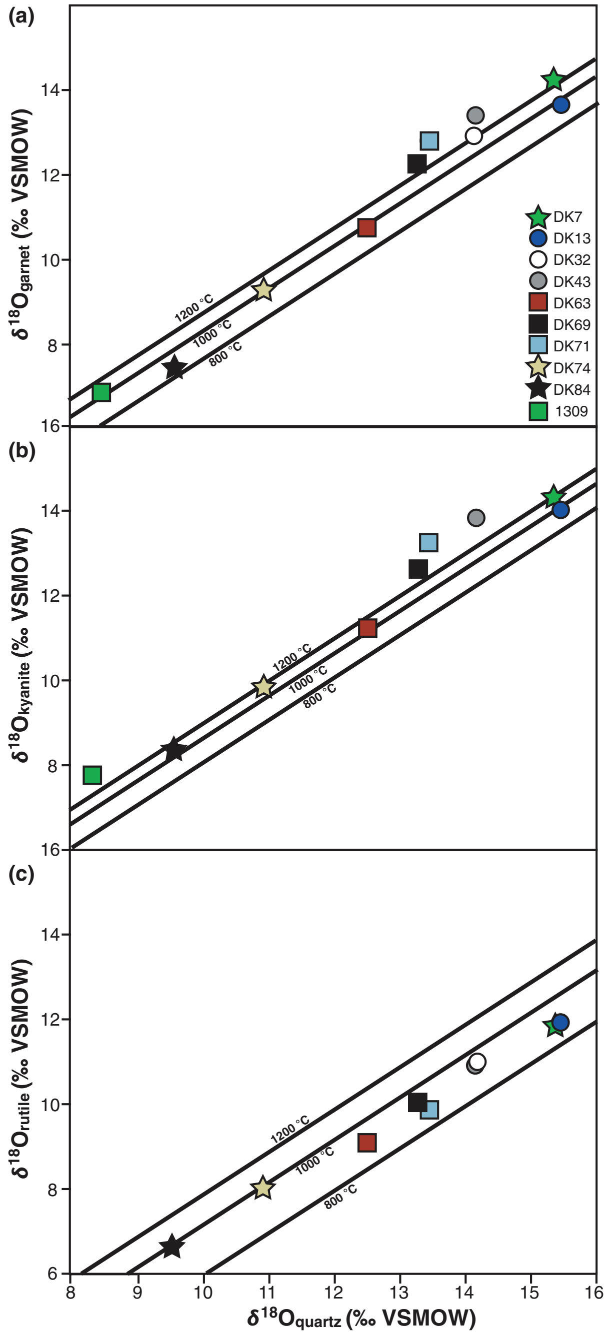

Fig. 4. Values of δ^{18}O laser fluorination (a) garnet, (b) kyanite and (c) rutile *v.* δ^{18}O(quartz) with isotherms at 200 °C intervals. Analytical uncertainties are smaller than the symbol size and are thus omitted.

Quartz δ^{18}O values show the smallest range of oxygen-isotope ratios, except for sample DK69 (Fig. 5c), for which ion-microprobe analyses reveal two populations, one ~13.7‰ and a second averaging 10.8‰. The latter, lighter values correspond to quartz grains found in a late alkali-feldspar + carbonate ribbon formed parallel to the foliation. Xenoliths

Table 2. Laser-fluorination oxygen-isotope analyses and calculated temperatures.

Sample	Rock type	δ^{18}O Grt (‰ VSMOW)	Average (‰ VSMOW)	2 SD[a] (‰ VSMOW)	δ^{18}O Qtz (‰ VSMOW)	Average (‰ VSMOW)	2 SD[a] (‰ VSMOW)	δ^{18}O Ky (‰ VSMOW)	Average (‰ VSMOW)	2 SD[a] (‰ VSMOW)	δ^{18}O Rt (‰ VSMOW)	Average (‰ VSMOW)	2 SD[a] (‰ VSMOW)	*T*(Grt-Qtz) (°C)	2 SD (°C)[b]	*T* (Ky-Qtz) (°C)	2 SD (°C)[b]	*T* (Rt-Qtz) (°C)	2 SD (°C)[b]
DK7	Granulite	14.3	14.30	0.17	15.28 15.42	15.35	0.17	14.3 14.39	14.35	0.17	11.89	11.86	0.17	1351	+223/−157	1223	+219/−152	885	+42/−38
DK13	Granulite	13.62 13.83	13.73	0.17	15.39 15.51	15.45	0.17	14.08 14.02	14.05	0.17	11.91 11.91	11.91	0.17	994	+97/−79	995	+125/−96	878	+41/−37
DK32	Eclogite	12.52 13.41	12.97	0.17	14.28 14.05	14.17	0.17				10.92 11.01	10.97	0.17	1246	+177/−131			937	+48/−43
DK43	Granulite	13.37 13.83	13.44	0.10	14.17 14.16	14.17	0.10	13.86 13.82	13.84	0.10	10.94 10.91	10.93	0.10	1674	+425/−162	2358	+866/−434	930	+27/−25
DK63	Granulite	10.89 10.75	10.82	0.17	12.63 12.4	12.52	0.17	11.29 11.16	11.23	0.17	9.12 9.11	9.12	0.17	1005	+100/−81	1048	+143/−108	901	+44/−39
DK69	Granulite	12.27 12.37	12.32	0.10	13.15 13.41	13.28	0.10	12.65 12.64	12.65	0.10	10.02 10.03	10.03	0.10	1425	+216/−111	1609	+252/−180	927	+27/−25
DK71	Granulite	12.87 12.91	12.89	0.10	13.43 13.45	13.44	0.10	13.22 13.31	13.27	0.10	9.82 9.94	9.88	0.10	1971	+139/−239	3313	+4549/−917	875	+23/−22
DK74	Granulite	9.42 9.24	9.33	0.17	10.88 10.9	10.89	0.17	9.74 9.96	9.85	0.17	8.05	8.05	0.17	1059	+354/−91	1198	+206/−145	1012	+58/−51
DK84	Eclogite	7.38 7.64	7.51	0.17	9.54 9.53	9.54	0.17	8.32 8.50	8.41	0.17	6.70 6.58	6.64	0.17	896	+75/−63	1141	+180/−130	1000	+56/−50
1309	Eclogite	6.80	6.80	0.20	8.40	8.40	0.20	7.70	7.70	0.20				1028	+201/−137	1520	+946/−363		

Temperatures were calculated using the temperature coefficients from Valley (2003).

[a] 2 SD uncertainties were calculated based on the analytical 2 SD uncertainty on the standard UWG-2.

[b] 2 SD temperature uncertainties were calculated by taking the square root of the sum of the squares of the uncertainties of the individual mineral analyses.

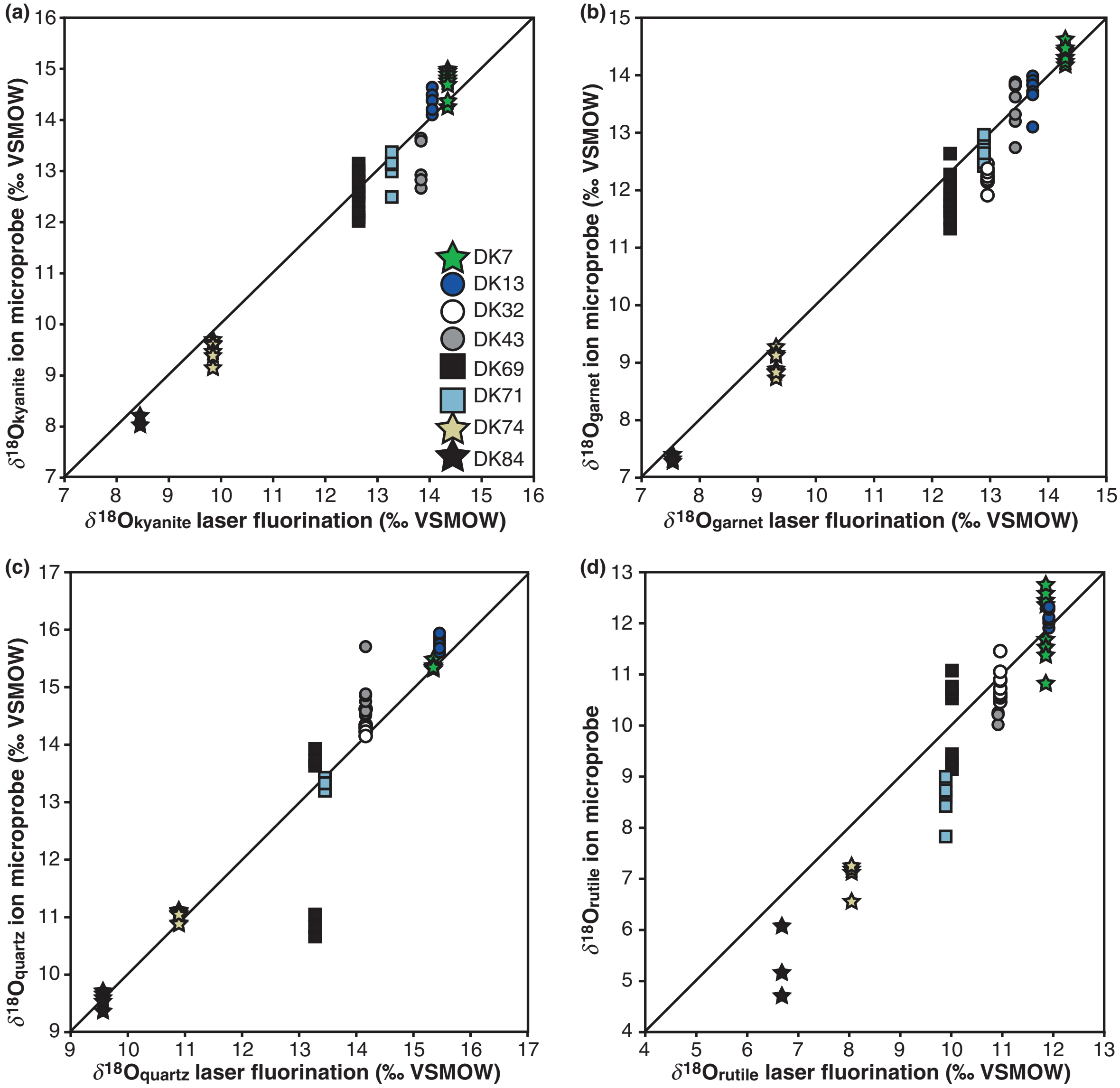

Fig. 5. Values of laser fluorination $\delta^{18}O$ *v.* ion microprobe $\delta^{18}O$ for (a) kyanite, (b) garnet, (c) quartz and (d) rutile. Note the heterogeneity found in the individual measurements. Rutile analyses by ion microprobe vary systematically from grain to grain due to orientation effects and are only accurate for assessing intra-mineral homogeneity.

Table 3. Average WiscSIMS ion-microprobe oxygen-isotope analyses and calculated temperatures.

Sample	Rock type	$\delta^{18}O$ Grt (%o VSMOW)	2 SD[a] (% VSMOW)	$\delta^{18}O$ Qtz (% VSMOW)	2 SD[a] (% VSMOW)	$\delta^{18}O$ Ky (% VSMOW)	2 SD[a] (% VSMOW)	$\delta^{18}O$ Zirc (% VSMOW)	2 SD[a] (% VSMOW)	$\delta^{18}O$ Rt (% VSMOW)
DK7	Granulite	14.28	0.31	15.38	0.32	14.81	0.31	14.30	0.32	12.62
DK13	Granulite	13.87	0.20	15.77	0.21	14.49	0.21	13.76	0.21	12.08
DK32	Eclogite	12.23	0.25	14.32	0.27					10.74
DK43	Granulite	13.25	0.38	14.69	0.39	13.60	0.39	13.59	0.41	10.17
DK69	Granulite	11.66	0.29			12.60	0.42	12.75	0.32	10.73
DK71	Granulite	12.68	0.45	13.40	0.27	13.15	0.27	12.87	0.22	8.80
DK74	Granulite	9.06	0.23	11.01	0.28	9.56	0.28	9.47	0.45	7.18
DK84	Eclogite	7.31	0.22	9.61	0.34	8.10	0.22	8.14	0.21	6.24

Temperatures are calculated using the temperature coefficients from Valley (2003).

[a] 2 SD uncertainties are calculated based on the analytical 2 SD uncertainty on the standard UWG-2.

[b] 2 SD temperature uncertainties are calculated by taking the square root of the sum of the squares of the uncertainties of the individual mineral analyses.

DK32 and DK43 each contain one heavier $\delta^{18}O$ quartz outlier; these are from quartz inclusions in garnet.

Of all the minerals, rutile reveals the broadest variability in the $\delta^{18}O$ raw values measured by ion microprobe (Fig. 5d). The heterogeneous nature of the measurements is mostly due to differences from grain to grain, which as described above is likely biased by crystal-orientation effects.

P–T estimates

Oxygen-isotope thermometry

Oxygen fractionation by a range of different mineral pairs (e.g. Zheng, 1993a,b; Chacko *et al.*, 2001; Valley, 2003) allows the potential of multiple temperatures to be obtained from a single sample. Thus, oxygen isotopes reveal either equilibrium temperatures or information concerning disequilibrium among minerals, which is crucial for interpreting *P–T* paths. However, the temperature sensitivity of most mineral pairs is poor at ultrahigh temperatures. For instance, at 1000 °C, even if both minerals are homogeneous, an uncertainty of 0.5‰ in fractionation between the minerals shifts temperature by $+128/-97$ °C for quartz–rutile, $+240/-153$ °C for quartz–garnet, $+317/-182$ °C for quartz–kyanite and $+301/-176$ °C for quartz–zircon pairs. In the xenoliths, there is local textural disequilibrium in areas affected by K-feldspar + carbonate metasomatism, and in DK32, relict kyanite suggests that at least some of the xenoliths have undergone decompression.

Even though the majority of the minerals appear to be texturally in equilibrium in the studied xenoliths, oxygen-isotope fractionation for the mineral pairs quartz–garnet, quartz–kyanite and quartz–zircon all yield geologically unrealistic temperatures and/or large uncertainties (see Appendix S2). The quartz–rutile pairs, however, yield the most precise temperatures at these high-grade conditions. The $\Delta^{18}O_{\text{quartz–rutile}}$ laser-fluorination values range from 2.84‰ in DK74 to 3.56‰ in DK71, indicating a relatively narrow range in temperatures of $1012 + 58/-51$ °C to $875 + 23/-22$ °C (Fig. 4c; for individual temperature results, see Table 2). A discussion of the other mineral pairs and their uncertainties can be found in Appendix S2.

The rutile oxygen-isotope results obtained by ion microprobe are more heterogeneous than those obtained by laser fluorination, and most likely reflect orientation effects in rutile (see Appendix S2 for a detailed discussion). Based on these observations, only the laser fluorination $T(\Delta^{18}O_{\text{quartz–rutile}})$ are used to evaluate the thermal history. However, the ion-microprobe analyses of rutile can accurately reflect zonation within single crystals. The ion-microprobe analyses indicate that most rutile is homogeneous within a single grain, supporting the use of laser-fluorination data to calculate temperature.

Major-element thermobarometry

To further evaluate the equilibrium conditions of the different xenoliths, major-element thermobarometry was applied to the samples that had an appropriate mineral assemblage. In this respect, it is important to determine which mineral compositions do reflect pre-eruption equilibrium. Volume diffusion of Fe and Mg during eruption is expected at length scales <10 μm (see Hacker *et al.*, 2005 for a more detailed discussion). Mineral zoning in DK32 and DK84 occurs within garnet and omphacite on a large scale (>50 μm) and therefore represents pre-eruption heterogeneity. The garnet zoning is slightly different in the two samples: DK32 shows a continuous increase in grossular and decrease in both almandine and pyrope from core to rim. The DK84 garnet has outward decreases in grossular and increases in pyrope, but in the outermost ~250–300 μm of the grain, the opposite trend is observed. Garnet zoning similar to that in DK32 was observed in another Dunkeldik eclogite xenolith by Hacker *et al.* (2005).

The intersection of net-transfer and ion-exchange reactions defines pre-eruption equilibration pressures and temperatures and was used for the thermobarometry. The near-rim compositions of garnet, clinopyroxene and feldspar (see mineral chemistry section) were used to calculate these reactions with THERMOCALC (Holland & Powell, 1998), assuming no Fe^{3+} in the minerals. If Fe^{3+} is present, the omphacite will take up more Fe^{3+} than the garnet and Fe–Mg exchange thermometry will predict lower temperatures. Conversely, this implies that temperatures derived from Fe–Mg exchange between garnet and clinopyroxene represent maxima if Fe^{3+} is ignored (Krogh Ravna & Paquin, 2003). Grains used for thermobarometry were carefully selected to avoid any visible signs of disequilibrium. Both the garnet–kyanite and the garnet–omphacite granulites typically contain multiple feldspars. Late, Or-rich (>97 mol.%) feldspar moats around kyanite were not used for thermobarometry. Instead, only coarse matrix feldspar in textural equilibrium with garnet and omphacite was used. Uncertainties in the major-element thermobarometry are a consequence of the assumption of equilibrium among the mineral assemblage, the accuracy and precision of the electron-microprobe analyses, and the calculations using THERMOCALC. The pressure and temperature from garnet–omphacite granulite DK32 have been estimated from Fe–Mg exchange between garnet and clinopyroxene and the net-transfer reaction albite = jadeite + quartz. These two reactions intersect at ~880 °C and 19 kbar (Fig. 6a). Kyanite is present in the sample, but its relict appearance suggests that it is no longer part of the equilibrium assemblage; this it was not used for thermobarometry.

For eclogite DK84, in which various garnet rim compositions have been observed, different garnet–

clinopyroxene pairs yield a wide range of temperatures. The Fe–Mg exchange reaction between garnet and clinopyroxene and the net-transfer reactions albite = jadeite + quartz and diopside + kyanite = grossular + quartz intersect at a pressure of ~18 kbar and 815 °C for one garnet–clinopyroxene pair (Fig. 6b) and ~24 kbar and 1025 °C for a second pair (Fig. 6c). These results further emphasize disequilibrium in DK84.

In comparison with the garnet–omphacite granulite DK32 and eclogite DK84, constraining the pre-eruption *P–T* conditions of the clinopyroxene-free granulites is severely limited by the fact that the assemblage garnet–kyanite–sanidine–quartz is stable over a broad *P–T* range (e.g. DK7; Fig. 7), within which mineral compositions change insignificantly. The only net-transfer reaction applicable to these rocks is 3 anorthite (in sanidine) = grossular + 2 kyanite + quartz (GASP; Ghent, 1976). However, the Ca exchange between garnet and alkali feldspar is negligible in the *P–T* range of interest (< 1 mol.% variation of anorthite and grossular; see pseudosection description below). The anhydrous nature of the samples suggests that they formed by dehydration melting of metapelites at > 900 °C (Patiño Douce & McCarthy, 1998), which yields a loose first-order temperature estimate. Oxygen-isotope equilibria thus provide the more reliable pre-eruption temperature estimates.

The pre-eruption pressure for granulite DK69 can be calculated using the GASP barometer; this reaction yields a pressure of 17 kbar using the $T(\Delta^{18}O_{quartz–rutile})$ of ~930 °C (see below). Feldspar-solvus thermometry can also be applied to DK69. At the ~17 kbar obtained from GASP, the calibration of Elkins & Grove (1990) yields ~925 °C (± 3 kbar uncertainty translates to a ± 8 °C uncertainty) for matrix plagioclase ($An_{29}Ab_{61}Or_{10}$) and sanidine ($An_{05}Ab_{29}Or_{66}$). Using the composition of feldspar rims ($An_{29}Ab_{46}Or_{25}$ and $An_{04}Ab_{26}Or_{70}$) included in garnet yields a higher temperature of ~1025 °C at ~17 kbar.

The pre-eruption *P–T* conditions of five garnet–phlogopite websterites were evaluated using equilibria among garnet, orthopyroxene and clinopyroxene. Here, we summarize the results; more details will appear in a separate paper (P. Luffi, unpublished data). Pressures and temperatures were calculated using the Al-in-orthopyroxene barometer of Nickel & Green (1985), based on the distribution of Al between garnet and orthopyroxene, in combination with the orthopyroxene–clinopyroxene solvus thermometer of Taylor (1998). Nimis & Grütter (2010) demonstrated that this is the most reliable method to assess equilibrium *P–T* conditions of fertile peridotites and pyroxenites. Only mineral analyses of adjacent grains were used. Results indicate that the websterites equilibrated in the 20–33 kbar/884–1012 °C range, which is similar to our estimates for the eclogite xenoliths. Individual samples yield core and rim *P–T* values that

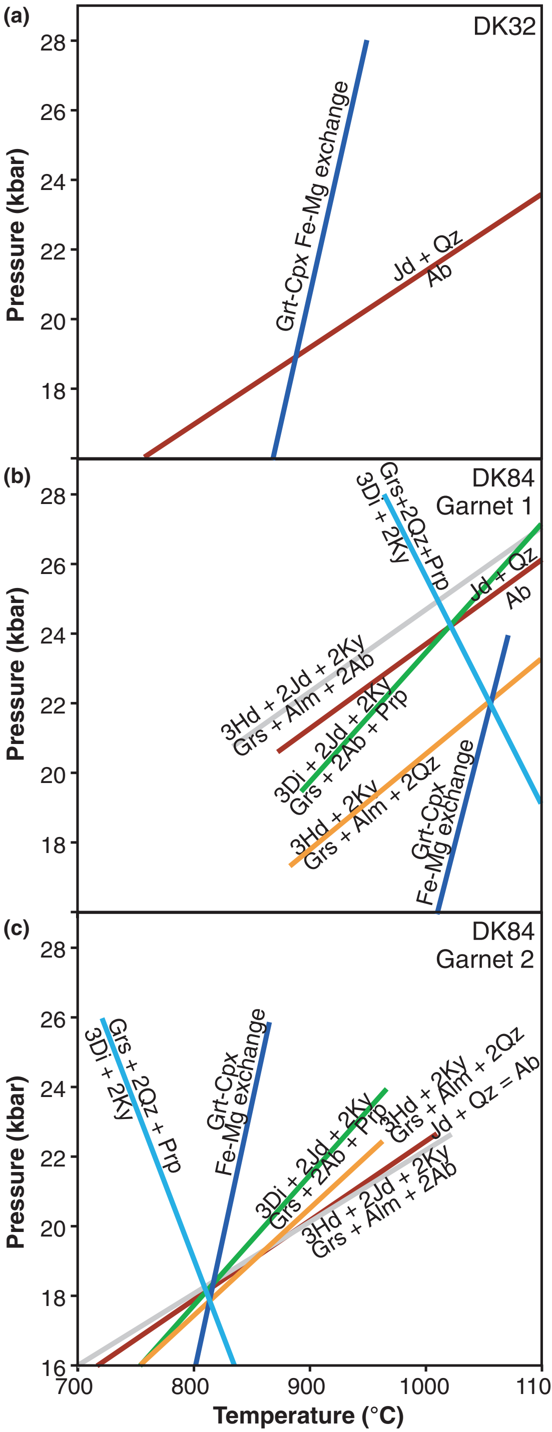

Fig. 6. Calculated pressures and temperatures for (a) garnet–omphacite granulite DK32, (b) eclogite DK84 grt 1, and (c) eclogite DK84 grt 2. Because DK84 attained only local equilibrium, plots (b) and (c) show reactions calculated using two different sets of adjacent grains of garnet, clinopyroxene and feldspar. All were calculated in the system $Na_2O–CaO–K_2O–FeO–MgO–Al_2O_3–SiO_2$. Ab = albite; Alm = almandine; Di = diopside; Grs = grossular; Hd = hedenbergite; Jd = jadeite; Ky = kyanite; Qz = quartz; Prp = pyrope.

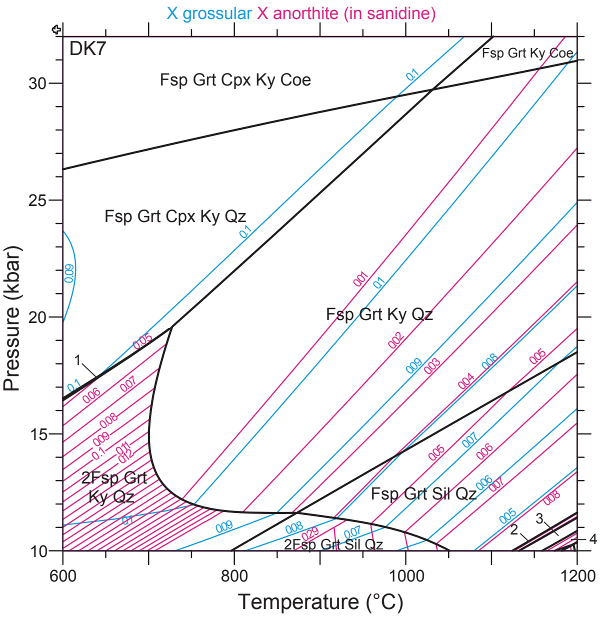

Fig. 7. Pseudosection for typical garnet–kyanite granulite DK7 calculated in the Na_2O–CaO–K_2O–FeO–MgO–Al_2O_3–SiO_2 system, showing broad stability field of garnet–kyanite–sanidine–quartz assemblage. (1) 2Fsp Grt Cpx Ky Qz; (2) Fsp Grt Sil Qz Spl; (3) Fsp Grt Qz Spl; (4) Fsp Grt Qz Spl Opx. Coe = coesite; Cpx = clinopyroxene; 2Fsp = plagioclase and alkali feldspar; Fsp = feldspar; Grt = garnet; Ky = kyanite; Qz = quartz; Opx = orthopyroxene; Sil = sillimanite; Spl = spinel.

are similar within calibration errors (±2 kbar, ±15–30 °C).

The garnet–biotite gneiss reveals the lowest *P–T* estimates of the sample suite. Both garnet core compositions + biotite inclusions in garnet and garnet rim compositions + adjacent matrix biotite give 790–850 °C for Fe–Mg exchange, using Holdaway & Lee (1977), Bhattacharya *et al.* (1992) and Perchuk & Lavrent'eva (1983).

Pseudosection calculations

The mineral assemblages dominating several of the studied xenoliths are not appropriate for determining the pre-eruption pressures via major-element thermobarometry. To place some constraints on such pressures, pseudosections were calculated using the bulk composition of the xenoliths. Such pseudosections reveal the *P–T* region in which the dominant mineral assemblages equilibrated (e.g. for the granulites, including DK7, Fig. 7). In addition, in the case of samples for which thermobarometric results have been calculated, such pseudosections can be used to evaluate the significance of the obtained pressures and temperatures and to show whether these values correspond to bulk or rather small-scale equilibrium. The pseudosections were calculated using Theriak/Domino 01.08.09 (De Capitani & Petrakakis, 2010) with the JUN92 thermodynamic database (based on end-member and solution models of Berman, 1988, 1991) completed with the omphacite solution model of Meyre *et al.* (1997) and the phengite solution model of Keller *et al.* (2005). To evaluate to what extent the topology of the obtained pseudosections depends on the chosen thermodynamic models in the *P–T* range of interest, we have also employed Perple_X 7 (Connolly & Petrini, 2002) with the Holland & Powell (1998) thermodynamic database, fitted with the garnet solution model of White *et al.* (2007), the feldspar solution model of Fuhrman & Lindsley (1988) and the omphacite model of Green *et al.* (2007).

The presented results (Figs 7–9 & S1) were calculated in Theriak/Domino; a pseudosection calculated with Perple_X for xenolith DK32 is shown in Fig. S2 for comparison. A comparison of Figs 8 & S2 corresponding to sample DK32 suggests that the pseudosections built with Theriak/Domino and Perple_X are similar in the *P–T* region of interest, and therefore insensitive to the employed thermodynamic models. Mineral abbreviations in the figures are after Whitney & Evans (2010), and several minor fields in the low-pressure/high-temperature region of the calculated pseudosections are too small to list the compositions and are labelled by numbers.

Whole-rock compositions used in these calculations are shown in Table 1; the models are calculated in the NCKFMAS (Na_2O–CaO–K_2O–FeO–MgO–Al_2O_3–SiO_2) system. To preserve consistency with the assumptions in the major-element thermobarometry, the pseudosections were calculated in Fe^{3+}-free systems. All pseudosections, except for DK83, were calculated without H_2O due to their anhydrous mineral assemblage. Due to the abundant biotite found in the thin section, it is assumed that DK83 does not represent a restite as interpreted for the other studied xenoliths. To equilibrate for the amount of biotite observed in DK83, 0.85 wt% H_2O was added to its bulk composition. Significantly more water would suppress the alkali feldspar observed in the assemblage; significantly less water would extend the stability of pyroxene against biotite and suppress the garnet–two-feldspar–biotite–quartz assemblage dominating this sample.

Uncertainties in the pseudosections are a consequence of the chosen activity models, the uncertainty in the thermochemical data, the assumption of equilibrium and the assumption that the chosen bulk composition is that with which all minerals equilibrated. In the ideal case of equilibrium, isopleths of the observed mineral rim compositions should intersect in a *P–T* point in an assemblage field that includes all the minerals in the sample. This is rarely the case in natural rocks, and samples containing zoned minerals, relict phases, evidence for metasomatism and/or two or more generations of a mineral, like the xenoliths studied here, will deviate from this ideal condition. Perhaps, the biggest limitation is that there is no

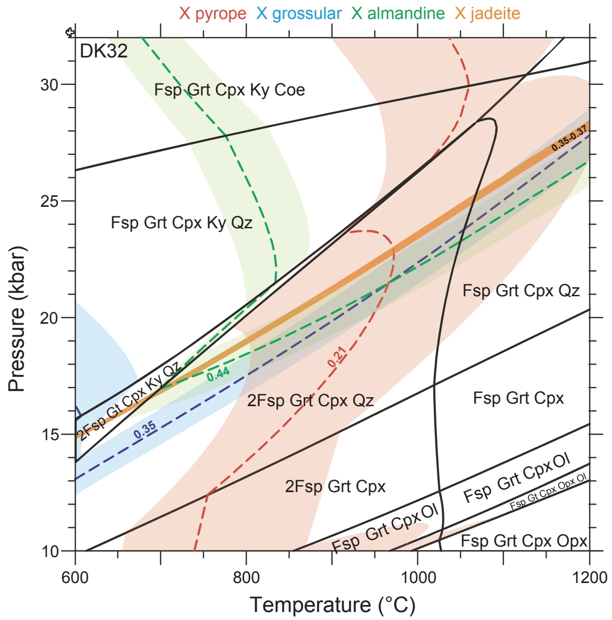

Fig. 8. Pseudosection and isopleths for almandine, grossular and pyrope for the garnet–omphacite granulite DK32 calculated in the Na_2O–CaO–K_2O–FeO–MgO–Al_2O_3–SiO_2 system; the molar isopleths of the rim garnet intersect at ~960–975 °C and 20–21 kbar. For the pseudosections for this sample and the eclogites, it was assumed that a small fraction of total Fe in omphacite is accommodated as Fe^{3+} and that the jadeite–aegirine binary be approximated as ideal. Because the Meyre *et al.* (1997) solution model excludes aegirine, the calculated jadeite mol. fraction is greater than analysed in the sample. The blue, red, green and orange bands correspond to ±1 mol.% uncertainty around grossular, pyrope, almandine and jadeite values observed in the garnet and clinopyroxene rims. Coe = coesite; Cpx = clinopyroxene; Fsp = feldspar; Grt = garnet; Ky = kyanite; Ol = olivine; Opx = orthopyroxene; Qz = quartz.

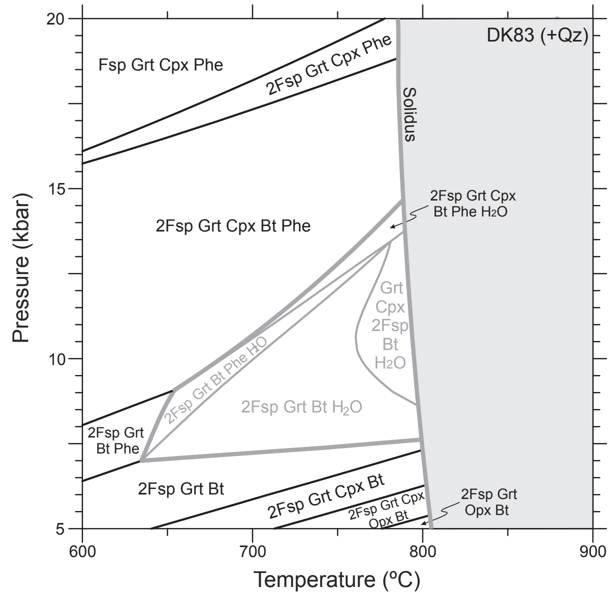

Fig. 9. Pseudosection for garnet–biotite gneiss DK83, calculated in the Na_2O–CaO–K_2O–FeO–MgO–MnO–Al_2O_3–SiO_2 system. Fields in grey are likely in the supersolidus region and are thus metastable with respect to melt. The solidus is based on a greywacke composition from Vielzeuf & Montel (1994) and Auzanneau *et al.* (2006). (1) Fsp Grt Cpx Phe Qz H_2O; (2) 2Fsp Grt Cpx Phe Qz H_2O; (3) 2Fsp Grt Cpx Bt Phe Qz H_2O; (4) 2Fsp Grt Cpx Opx Bt Qz H_2O; (5) 2Fsp Grt Bt Phe Qz H_2O; (6) 2Fsp Grt Bt Phe Qz; (7) 2Fsp Grt Cpx Opx Bt Qz; (8) 2Fsp Grt Opx Bt Qz; (9) Fsp Grt Cpx Phe Ky Coe; Coe = coesite; Cpx = clinopyroxene; Fsp = feldspar; Grt = garnet; Ky = kyanite; Opx = orthopyroxene; Qz = quartz; Phe = phengite.

internally consistent set of activity models nor a thermodynamic database for silicate melts for the compositions, high pressures and temperatures of interest.

For granulite DK32, the molar isopleths of grossular, almandine and pyrope rim compositions intersect at ~960–975 °C and 20–21 kbar in the equilibrium assemblage of garnet–clinopyroxene–sanidine–plagioclase–quartz–(rutile) (Fig. 8). DK32 also contains kyanite, but the presence of feldspar rims around kyanite and the fact that eclogites from this same xenolith suite record higher pressures and temperatures (Hacker *et al.*, 2005) suggest that the kyanite is relict and that DK32 cooled and decompressed from the sanidine–kyanite–clinopyroxene–garnet–quartz stability field. The core-composition isopleths of the garnet intersect at unrealistically high temperatures above those shown on the pseudosection.

Estimating the pre-eruption *P–T* conditions for eclogite DK84 is difficult because the garnet has different rim compositions (Fig. 3a), indicating that only local equilibrium has been achieved. Further complications arise from the presence of secondary alkali feldspar and sanidine not equilibrated with the primary assemblage. These factors explain why the molar isopleths for garnet do not intersect within the calculated stability field for the assemblage observed in the xenolith (Fig. S1).

The pseudosection constructed for garnet–biotite gneiss DK83 is shown in Fig. 9. According to Theriak/Domino, garnet, phengite, omphacite and alkali feldspar are stable in the low-temperature–high-pressure domain of the examined *P–T* range. There is a *P–T* field (600–840 °C and 5–14 kbar) in which the assemblage two feldspars–quartz–biotite–garnet ± H_2O is stable. In the case of DK83, the model is limited by uncertainties in the H_2O contents in the rock (here estimated by the modal biotite) and, thereby, by the approximate constraints on the solidus position. Nevertheless, the temperature range of stability of the observed assemblage estimated from the pseudosection is consistent with conventional thermometry results from this sample. Thus, we conclude that DK83 must have equilibrated somewhere in the 5–14 kbar range.

Metamorphic pressures

To determine metamorphic pressures in samples for which major-element thermobarometry was not possible, we combine the oxygen-isotope quartz–rutile temperatures and the calculated stability field of the mineral assemblages. To ensure that results of such a combination are meaningful, the oxygen-thermometry results are first compared with the major-element thermometry and pseudosections. Individual samples yield consistent temperatures for all of the techniques. For example, for garnet–omphacite granulite DK32, major-element thermobarometry indicates ~890 ± 70 °C/19 ± 2 kbar, the pseudosection yields ~960–975 ± 70 °C/20–21 ± 4 kbar and laser fluorination $T(\Delta^{18}O_{quartz–rutile})$ = 940 ± 45 °C. The uncertainties associated with the thermobarometry and pseudosection *P–T* estimates are similar to those of the quartz–rutile thermometry, and the overall results suggest a pre-eruption *P–T* condition of 900 °C/20 kbar. Exchange thermometry serves as a check for the oxygen-derived temperatures for granulite DK69. Feldspar-solvus thermometry yielded a temperature of 925 ± 50 °C, whereas laser fluorination resulted in $T(\Delta^{18}O_{quartz–rutile})$ = 930 ± 42 °C. In conclusion, the results from both DK32 and DK69 suggest that the quartz–rutile $T(\Delta^{18}O)$ temperatures can be directly applied to the samples not suitable for conventional thermometry.

For most samples, the mineral assemblage stability field is large (e.g. DK7, Fig. 7). For granulite DK13, $T(\Delta^{18}O_{quartz–rutile})$ = 877 °C superposed on the stability field of garnet + sanidine + kyanite + quartz indicates a pressure of 12–25 kbar. For DK43, $T(\Delta^{18}O_{quartz–rutile})$ = 930 °C, the same mineral assemblage indicates 13–26 kbar. Xenolith DK71 has a laser-fluorination $T(\Delta^{18}O_{quartz–rutile})$ of 875 °C, corresponding to a pressure of 12–25 kbar. At $T(\Delta^{18}O_{quartz–rutile})$ = 1011 °C, the garnet–sanidine–kyanite–quartz–rutile assemblage of DK74 is stable at 15–29 kbar. DK69 is the only clinopyroxene-free garnet–kyanite granulite for which a pre-eruption pressure can be determined. This sample equilibrated at ~930 °C, and on the pseudosection, falls in the same pressure range as the other granulites (13–26 kbar); the GASP barometer yields a more precise pressure of 17 kbar. Finally, the 790–850 °C cation-exchange temperature inferred for the garnet–biotite gneiss (DK83) indicates a pressure < 14 kbar, based on the pseudosection (Fig. 9). Overall, the equilibrium pressures for the granulites lacking clinopyroxene range from ~12 kbar (the stability field of kyanite) up to the clinopyroxene-in boundary (~25 kbar at 900 °C).

Depth-profiling U–Pb zircon analyses

Zircon U–Pb SHRIMP depth-profiling analyses were obtained from xenoliths DK32 and DK84 (Table S4). The depth-profiling technique may allow acquisition of the isotopic signature of the last event to affect zircon and thus may indicate the pre-eruption age of the zircon. The unpolished rims of 15 zircon analysed from the granulite DK32 yielded a lower intercept date of 19.9 ± 3.3 Ma (Fig. 10a). The zircon dates from eclogite DK84 are more scattered: most of the 20 zircon analysed yielded $^{238}U/^{206}Pb$ rim dates from 97.6 ± 3.7 to 23.6 ± 1.0 Ma (Table S4), whereas five zircon yielded a lower intercept date of 12.9 ± 1.0 Ma (Fig. 10b), indistinguishable from the eruption age of 11.5 ± 0.2 Ma (Hacker *et al.*, 2005), given current uncertainties in intercalibration of the U–Pb and K–Ar decay schemes (Renne *et al.*, 2010).

DISCUSSION

Origin of the Dunkeldik xenoliths

The origin of the Dunkeldik xenoliths is partly obscured by partial melting and infiltration that produced potassium feldspar + carbonate. However, oxygen isotopes measured from the xenoliths provide insight into the fluid–rock interaction history. The $\delta^{18}O$ values measured from all the minerals in the studied xenoliths are heavy compared to mantle values, with the weighted-mean values for quartz ranging from 9.5‰ to 15.4‰. These heavy $\delta^{18}O$ signatures – including those from garnet cores – mean that even the eclogites DK84 and 1309 must have been altered at shallow crustal depths or have a metasedimentary protolith (most mafic eclogite xenoliths have $\delta^{18}O$ values lighter than +9.0‰; e.g. Garlick *et al.*, 1971; Deines *et al.*, 1991; Jacob *et al.*, 1994; Schulze *et al.*, 2003b). The oxygen-isotope data for the granulites lacking clinopyroxene are consistent with the metasedimentary origin inferred from the bulk chemistry of the samples [molar $Al_2O_3 > (CaO + Na_2O + K_2O)$; Table 1], mineral parageneses, melting history (Hacker *et al.*, 2005) and zircon ages (Ducea *et al.*, 2003). The xenolith suite thus covers a range of crustal rocks that have magmatic and sedimentary protoliths.

Pre-eruption *P–T* conditions

Most of this study focuses on the understanding of the last *P–T* conditions of the various xenoliths prior to their eruption. Textures in the samples argue that the xenoliths were not greatly affected by the host magma during transport to the surface. In addition, ascent rates of the xenoliths are expected to be ~0.1–3 m s^{-1} (Spera, 1984), and thus, the xenoliths are thought to have cooled rapidly (<<1 year) to below their closure temperatures for oxygen diffusion. In such conditions, re-equilibration is unlikely during eruption (Hacker *et al.*, 2005) because grain-boundary and volume diffusion in the xenoliths and constituent minerals are expected to be slow even at magmatic temperatures (<1000–1200 °C; e.g. Yund, 1997; Ganguly *et al.*,

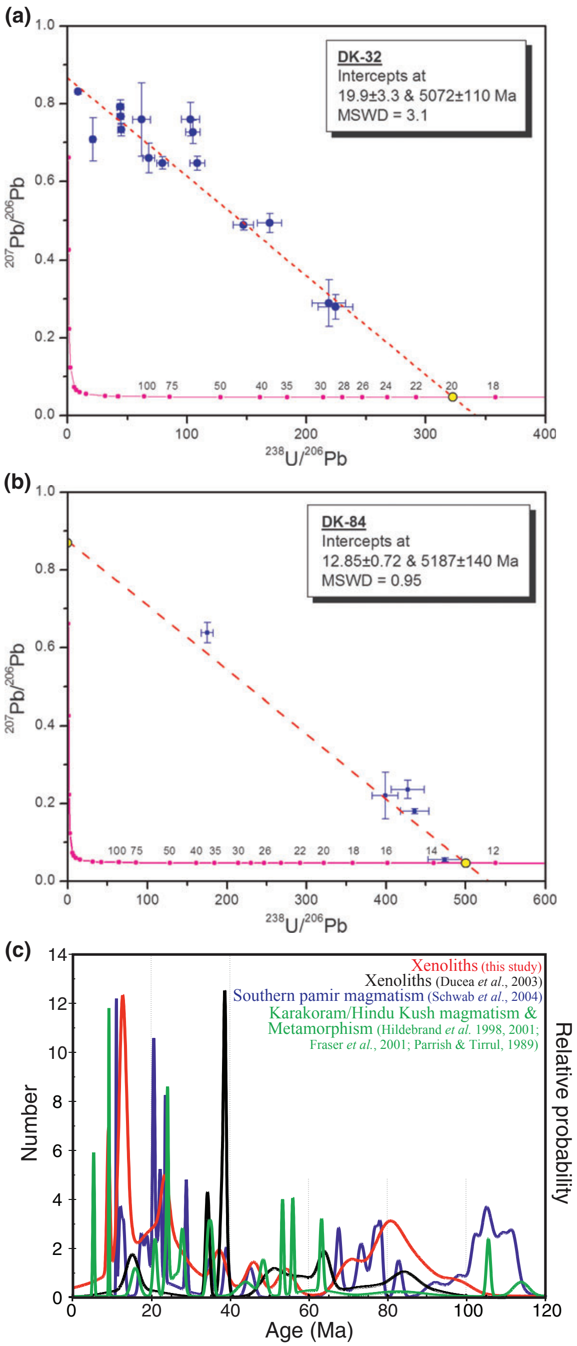

Fig. 10. Tera–Wasserburg plots generated using ISOPLOT 3.00 (Ludwig, 2003) of zircon SHRIMP depth-profiling results from (a) garnet–omphacite granulite DK32 and (b) eclogite DK84. Each plot represents a single depth-profiling analysis with its associated error; (c) U–Pb xenolith zircon and monazite ages (this study; Ducea *et al*., 2003) compared with U–Th–Pb zircon, monazite, xenotime and uraninite ages from the southern Pamir, eastern Hindu Kush and the Karakoram.

1998; Dimanov & Sautter, 2000; Cole & Chakraborty, 2001; Milke *et al*., 2001; Valley, 2001; Page *et al*., 2007a,b). For oxygen diffusion, closure temperatures are estimated at > 1500 °C and diffusion distances are < 5 μm for all the analysed phases assuming the fast cooling/eruption rates and using the diffusion characteristics summarized by Valley (2001) and Cole & Chakraborty (2001). Thus, the elemental and isotopic measurements used in this study are considered the representatives of the pre-eruption conditions and not affected by the magma during eruption.

Thermobarometry results from this study and Hacker *et al*. (2005) suggest a broad range of pre-eruption *P*–*T* conditions for the Dunkeldik xenolith suite (Fig. 11). The anhydrous granulites and eclogites yield conditions from ~815 °C at 18 kbar to 1100 °C at 28 kbar and the garnet–biotite gneiss yields 790–850 °C at pressures between 5 and 14 kbar. The websterites appear to have equilibrated at temperatures that overlap those of the eclogites and granulites; however, the pressures recorded in the websterites appear to be 5–10 kbar greater.

The *P*–*T* results, combined with the dearth of hydrous phases in most of the xenoliths, corroborate the earlier view (Hacker *et al*., 2005) that the Dunkeldik xenoliths underwent partial melting and that the granulites with a metasedimentary protolith represent the residue of this melting. The absence of hydrous minerals – combined with the bulk composition – suggests that temperatures were > 900 °C for most of the xenolith suite (Patiño Douce & McCarthy, 1998). The single garnet–biotite gneiss is an outlier and represents the coldest end of the suite.

Whereas most of the xenoliths record high-grade pressures and temperatures, several samples reveal evidence of decompression and/or cooling prior to eruption. As described above, xenolith DK32 contains relict kyanite that is not in equilibrium with the two-feldspar–quartz–clinopyroxene–garnet assemblage. This relationship suggests that DK32 left the stability field of sanidine–kyanite–clinopyroxene–garnet–quartz (an assemblage observed in other eclogite xenoliths from Dunkeldik) via decompression and, probably, cooling. Eclogite DK84 also contains evidence for decompression prior to eruption. It yields multiple pressures and temperatures from garnet with different rim compositions, presumably reflecting cooling and decompression from 1025 °C/24 kbar to 815 °C/18 kbar. Finally, we interpret the granulites as melting residues, and in order for these rocks to have undergone phengite and biotite consumption, they must have reached > ~1050 °C (at > 20 kbar; Patiño Douce & McCarthy, 1998); however, many of the samples record lower temperatures, again suggesting cooling. Granulite DK69 also records multiple temperatures, with garnet inclusions yielding > 1000 °C, whereas the matrix yields a lower temperature near 900 °C.

Miocene Pamir lithosphere

The xenolith pressures of ~19–33 kbar indicate that crustal material, represented by Miocene eclogites, granulites and websterites, was taken to mantle depths

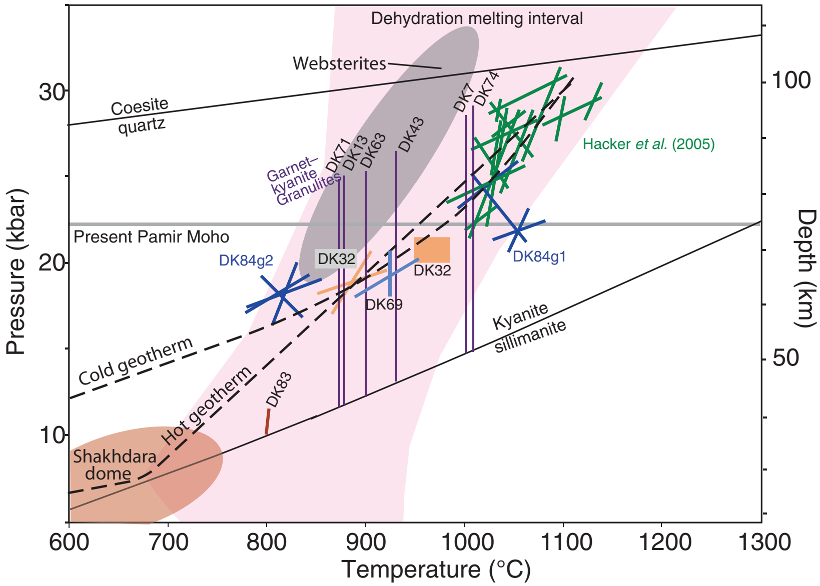

Fig. 11. *P–T* diagram for all of the studied eclogites, granulites and the garnet–biotite gneiss. Lines for samples DK32 and DK84 show the garnet–clinopyroxene thermometer, garnet + quartz = clinopyroxene + kyanite thermometer and the albite-breakdown barometer calculated using THERMOCALC. The black box for DK32 represents the *P–T* conditions based on the intersection of rim isopleths on the pseudosection computed by Domino, using the thermodynamic models of Berman (1988, 1991). Granulite temperatures are from quartz–rutile oxygen-isotope thermometry and the pressure range is from pseudosections computed using Domino. The DK83 gneiss temperature is derived from garnet–biotite Fe–Mg exchange and pressure is derived from the pseudosection computed by Domino. The darker grey-scale ellipse represents the pressures and temperatures calculated for the websterites. The lighter grey-scale ellipse shows the *P–T* range represented in the Pamir Mountains gneiss domes (McGraw *et al*., 2010). The dehydration-melting interval is from experiments by (Vielzeuf & Holloway, 1988; Vielzeuf & Montel, 1994; Montel & Vielzeuf, 1997; Patiño Douce & Harris, 1998; Schmidt *et al*., 2004; Patiño Douce, 2005; Auzanneau *et al*., 2006).

(∼65–110 km). Late Mesozoic zircon and monazite ages from the xenoliths (Fig. 10c; this study, Ducea *et al*., 2003) preclude derivation of the xenoliths from Indian crust (e.g. Hodges, 2000) and suggest instead an affinity to the southern Pamir–eastern Hindu Kush–Karakoram–Kohistan–Ladakh continental and oceanic arc rocks of southern Asia (e.g. Parrish & Tirrul, 1989; Hildebrand *et al*., 1998, 2001; Fraser *et al*., 2001). In particular, the protracted Tertiary high-grade thermal and magmatic history of the Hindu Kush, Karakoram and southern Pamir appears to be reflected in the xenoliths (Fig. 10c).

Using the six investigated garnet–omphacite granulite and eclogites from this study and from Hacker *et al*. (2005), the rocks define a geotherm of 12–13 °C km^{-1} in the 65–110 km depth range (cold geotherm of Fig. 11). The metasedimentary xenoliths are compositionally similar to Barrovian metamorphic rocks exposed in the nearby, southwestern Pamir Shakhdara gneiss dome (Fig. 1c) that reached peak pressures of 8–12 kbar and temperatures of 675–800 °C (Fig. 11; McGraw, 2010). Metamorphism in the Shakhdara dome is Miocene and older (McGraw *et al*., 2010; Stearns *et al*., 2011). Similar metamorphic and magmatic ages characterize the basement domes of the eastern Hindu Kush and Karakoram to the south of the Pamir Mountains (Fig. 10c). They reflect a protracted tectonothermal reworking of the upper and middle crust of the southern Asian plate margin, which is contemporaneous with the UHT–(U)HP metamorphism, melting, and subsequent decompression and cooling of the lower crust, reflected by the xenoliths.

The lower crust of continental cratons can be cold (<500 °C at 40 km; average thermal gradient of 12.5 °C km^{-1}; Hyndman, 2010), whereas thermal gradients in continent–continent collisions can be as steep as 25–40 °C km^{-1} (hot geotherm of Fig. 11; e.g. Lee *et al*., 2004; Root *et al*., 2005; Hyndman, 2010). The relatively low ratio of heat conduction to advection in Earth's crust means that a typical continent–continent collision is characterized by shallow thermal gradients during thickening stages and by steep thermal gradients during thinning stages (Oxburgh & Turcotte, 1974). For example, during the Miocene, the lower crust of southern Tibet was characterized by a thermal gradient of ∼16 °C km^{-1} (1130–1330 °C/22–26 kbar), as defined by felsic and mafic crustal xenoliths similar to those analysed for this study that were erupted in an ultrapotassic dyke (Chan *et al*., 2009). In comparison, the lower crust of the central Tibetan Plateau is now hot (>1000 °C at 40 km depth, ∼25 °C km^{-1}; Hacker *et al*., 2000), and development of that steep thermal gradient may have required 50 Ma of thermal relaxation assisted by radiogenic heating (LePichon *et al*., 1997; McKenzie & Priestley, 2008) or magmatic input (e.g. Ding *et al*., 2003). Over the same time interval, the southern Tibetan Plateau remained refrigerated by subduction (Hetenyi *et al*., 2007).

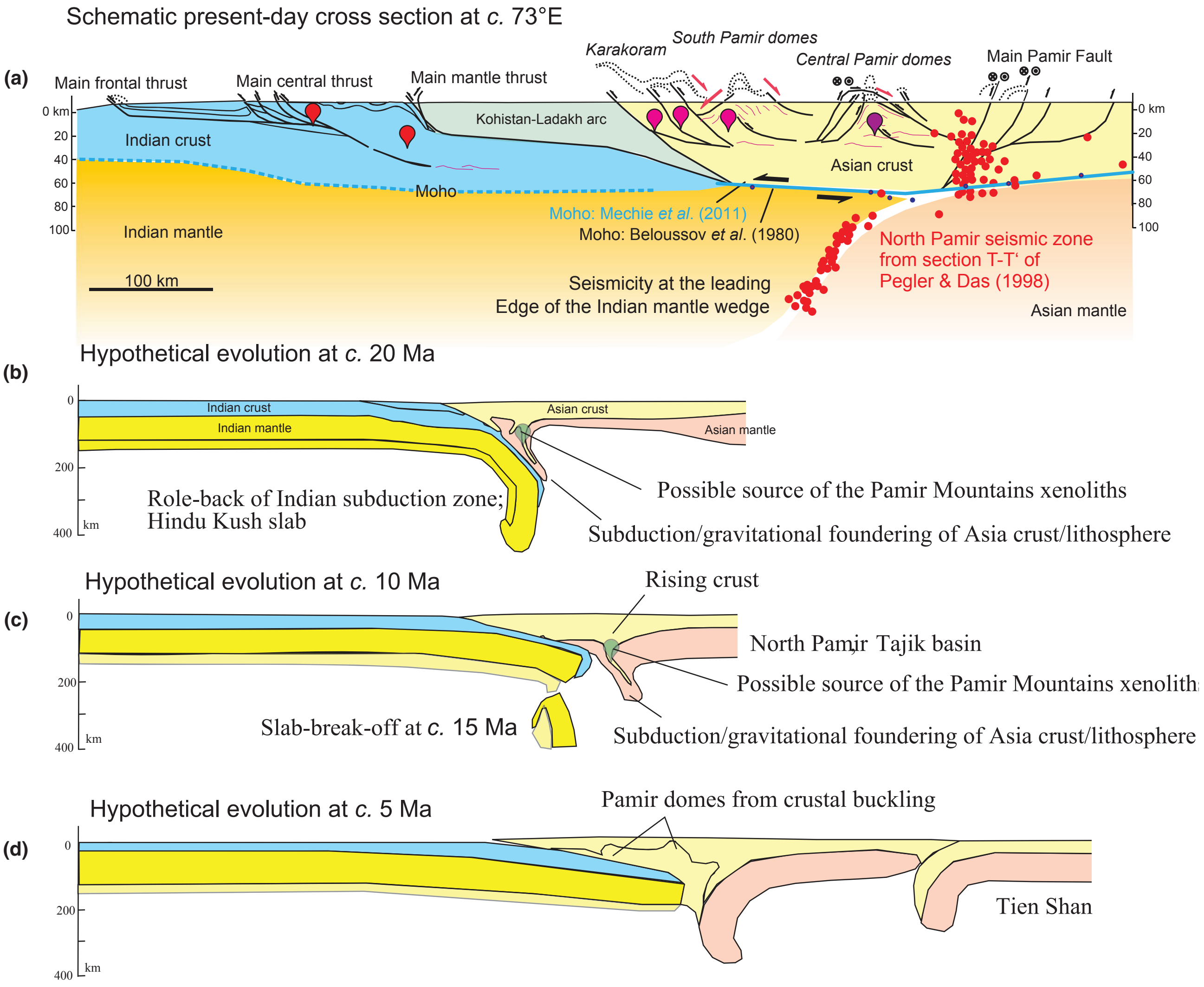

Fig. 12. Schematic N–S cross-section of the India–Asia collision zone with speculative deep extrapolation along ~73°E. The cross sections represent different times in the Pamir Mountains evolution from the (a) present day, (b) *c.* 20 Ma, (c) *c.* 10 Ma and (d) *c.* 5 Ma. The location of the possible source material for the xenoliths is indicated within the cross-section, and figure (a) shows the seismic data used for interpretations of the deep roots of the Pamir Mountains.

In light of these considerations, the fact that the Pamir Mountains xenoliths define an average thermal gradient of 12–13 °C km^{-1} (Fig. 11) in a collisional orogen indicates that they had not reached thermal equilibrium corresponding to a mature continent–continent collision. Instead, the results support the view that the crustal material reached ~1000–1100 °C at >90 km prior to decompressing and cooling to lower pressures and temperatures of ~800–900 °C/18 kbar and then being entrained in their host magma. This inference is supported by features of the xenoliths described above, such as oxygen-isotope disequilibrium and multiple compositions of garnet within a single thin section.

How the crustal material reached depths in the Miocene greater than the present-day Moho (~65 km depth for the southern Pamir; Mechie *et al.*, 2011) remains an open question. U–Pb zircon data suggest that the material most likely was ablated from the Asian upper plate during the subduction of India (Ducea *et al.*, 2003; Hacker *et al.*, 2005). Alternatively, it may have been introduced to the mantle by intracontinental subduction (Meyer *et al.*, 1998) or could have sunk into the mantle owing to a gravitational instability (Hacker *et al.*, 2005). We exclude DK83, the garnet–biotite gneiss, from consideration in these models because it equilibrated at shallower pressure than the other xenoliths; it was probably located within the mid-crust and collected during eruption.

As described, the *P–T* history recorded in the eclogitic and granulitic xenoliths implies that the crustal material did not fully equilibrate at peak pressures and temperatures or if the samples did, the record of that equilibration was obliterated by the decompression and cooling. Thus, the samples must have reached maximum depths and then decompressed/cooled potentially via buoyancy-driven exhumation after melting and melt extraction but prior to the eruption of the xenoliths at *c*. 11.5 Ma. In the gravitational instability model, the denser part of the descending body may have sunk into the mantle, whereas the felsic rocks separated from the dense lithologies and rose buoyantly. In the subduction model, felsic material could have been carried downward with the dense, subducting plate until heating decreased its viscosity sufficiently to allow diapiric rise of the felsic material through the overlying mantle wedge (e.g. Gerya & Yuen, 2003; Keppie *et al*., 2009; Behn *et al*., 2011).

Our preferred model (Fig. 12) for the Neogene to recent crustal and lithospheric mantle evolution beneath the southern Pamir calls for early Miocene steep subduction of Indian lithosphere beneath the southern Pamir region, similar to the present-day Hindu Kush slab. This induced local subduction erosion or gravitational foundering of Asian crust, which served as the protolith for the Pamir Mountains xenoliths. The deeply subducted Indian lithosphere slab subsequently broke off. Since the Late Miocene, Indian mantle lithosphere has been underthrusting nearly horizontally, effectively cooling the overlying Asian crust. The leading edge of India is currently outlined by the Pamir Mountains seismic zone (Fig. 1b). This underthrusting Indian mantle lithosphere probably corresponds to the cool upper mantle underneath the inferred from wide-angle seismic data Pamir (Mechie *et al*., 2011).

CONCLUSIONS

Ultrapotassic volcanic rock in the southeast Pamir contains crustal xenoliths scavenged from depths of ~40 km (garnet–biotite gneiss) to ~90 km (eclogites, granulites and websterites), with most of the granulites, eclogites and websterites intermingled at 60 to 100 km depths. Most of these samples achieved ultrahigh-temperatures of 1000–1100 °C, leading to mica-dehydration melting. The resulting UHT–near-UHP xenoliths represent the residue of these melts and define an average thermal gradient of 12–13 °C km^{-1} for depths of 60–100 km. Thermobarometry suggests that the eclogites and granulites cooled and decompressed from >1000 °C to ~900 °C before eruption. The xenoliths may have reached great depth through subduction erosion, intracontinental subduction or a smaller gravitational instability. Regardless, the thermobarometry, oxygen-isotope data and textures indicate that the rocks did not thermally equilibrate at temperatures expected for these depths, but instead cooled to ~900 °C. The xenoliths provide a rare window into the fate of crustal material taken to mantle depths and highlight the dehydration melting and subsequent cooling/decompression that occurs when the crustal material reaches *P–T* conditions at which phengite/biotite are no longer stable.

ACKNOWLEDGEMENTS

This study was funded by National Science Foundation Grant EAR-0742451 to B. Hacker and P. Kelemen and DFG Grant RA442/34 to L. Ratschbacher. The WiscSIMS ion-microprobe laboratory is partly supported by National Science Foundation Grants (EAR-0319230, -0744079 and -1053466). We thank G. Seward for his help and guidance in using the electron microprobe and SEM at UCSB. M. Grove was of great assistance in collecting the depth-profiling U–Pb and Ti-in-zircon data at Stanford University. We also thank J. Huberty for his analyses and development of the kyanite and rutile standards used for the ion microprobe δ^{18}O analyses and discussions about orientation effects during ion-microprobe analysis of oxygen-isotope ratios in rutile and Fe-oxides. C. Twarz and B. Schurr helped to compile Fig. 1a,b. This manuscript benefited from thoughtful comments by reviewers C. Warren and L. Tajcmanová.

REFERENCES

Auzanneau, E., Vielzeuf, D. & Schmidt, M.W., 2006. Experimental evidence of decompression melting during exhumation of subducted continental crust. *Contributions to Mineralogy and Petrology*, **152,** 125–148.

Barth, A.P. & Wooden, J.L., 2010. Coupled elemental and isotopic analyses of polygenetic zircons from granitic rocks by ion microprobe, with implications for melt evolution and the sources of granitic magmas. *Chemical Geology*, **277,** 149–159.

Behn, M.D., Kelemen, P.B., Hirth, G., Hacker, B.R. & Massonne, H.-J., 2011. Diapirs as the source of the sediment signature in arc lavas. *Nature Geoscience*, **4,** 641–646.

Beloussov, V.V., Belyaevsky, N.A., Borisov, A.A. *et al*., 1980. Structure of the lithosphere along deep seismic sounding profile: Tien Shan–Pamirs–Karakorum–Himalayas. *Tectonophysics*, **70,** 193–221.

Berman, R.G., 1988. Internally-consistent thermodynamic data for minerals in the system Na_2O–K_2O–CaO–MgO–FeO–Fe_2O_3–Al_2O3–SiO_2–TiO_2–H_2O–CO_2. *Journal of Petrology*, **29,** 445–522.

Berman, R.G., 1991. Thermobarometry using multiequilibrium calculations: a new technique with petrological applications. *Canadian Mineralogist*, **29,** 833–856.

Bhattacharya, A., Mohanty, L., Maji, A., Sen, S.K. & Raith, M., 1992. Non-ideal mixing in the phlogopite-annite binary: constraints from experimental data on Mg-Fe partitioning and a reformulation of the biotite–garnet geothermometer. *Contributions to Mineralogy and Petrology*, **111,** 87–93.

Breeding, C.M., Ague, J.J., Grove, M. & Rupke, A.L., 2004. Isotopic and chemical alteration of zircon by metamorphic fluids: U-Pb age depth-profiling of zircon crystals from Barrow's garnet zone, northeast Scotland. *American Mineralogist*, **89,** 1067–1077.

Chacko, T., Cole, D.R. & Horita, J., 2001. Equilibrium oxygen, hydrogen, and carbon isotope fractionation factors applicable to geologic systems. In: *Stable Isotope Geochemistry* (eds Valley, J.W. & Cole, D.R.), *Reviews in Mineralogy and Petrology*, **43,** 1–81.

Chan, G.H.-N., Waters, D.J., Searle, M.P. *et al*., 2009. Probing the basement of southern Tibet: evidence from crustal xenoliths entrained in a Miocene ultrapotassic dyke. *Journal of Geological Society*, **166,** 45–52, doi: 10.1144/0016-76492007-145.

Clayton, R.N., Goldsmith, J.R., Kavel, K.J., Mayeda, T.K. & Newton, R.C., 1975. Limits on the effect of pressure on isotopic fractionation. *Geochimica Cosmochimica Acta*, **39,** 1197–1201.

Cole, D.R. & Chakraborty, S., 2001. Rates and mechanisms of isotopic exchange. In: *Stable Isotope Geochemistry* (eds Valley, J.W. & Cole, D.R.), *Reviews in Mineralogy and Geochemistry*, **43,** 83–224.

Connolly, J.A.D. & Petrini, K., 2002. An automated strategy for calculation of phase diagram sections and retrieval of rock properties as a function of physical conditions (0.4 Mb). *Journal of Metamorphic Geology*, **20,** 697–708.

De Capitani, C. & Petrakakis, K., 2010. The computation of equilibrium assemblage diagrams with Theriak/Domino software. *American Mineralogist*, **95,** 1006–1016.

Deines, P., Harris, J.W., Robinson, D.N., Gurney, J.J. & Shee, S.R., 1991. Carbon and oxygen isotope variations in diamond and graphite eclogites from Orapa, Botswana, and the nitrogen content of their diamonds. *Geochimica Cosmochimica Acta*, **55,** 515–524.

Dimanov, A. & Sautter, V., 2000. 'Average' interdiffusion of (Fe, Mn)–Mg in natural diopside. *European Journal of Mineralogy*, **12,** 749–760.

Ding, L., Kapp, P., Zhong, D. & Deng, W., 2003. Cenozoic volcanism in Tibet: evidence for a transition from oceanic to continental subduction. *Journal of Petrology*, **44,** 1833–1865.

Dmitriev, E.A., 1976. *Kainozoiskie kalievye schelochnye porody Vostochnogo Pamira (Cenozoic potassic rocks of eastern Pamir)*. Akademiya Nauk Tadzhikskoy SSR, Dushanbe, 171 pp.

Ducea, M.N., Lutkov, V., Minaev, V.T. *et al*., 2003. Building the Pamirs: the view from the underside. *Geology*, **31,** 849–852.

Elkins, L.T. & Grove, T.L., 1990. Ternary feldspar experiments and thermodynamic models. *American Mineralogist*, **75,** 544–559.

Engdahl, E.R., van der Hilst, R. & Buland, R., 1998. Global teleseismic earthquake relocation with improved travel times and procedures for depth determination. *Bulletin Seismological Society of America*, **88,** 722–743.

England, P.C. & Thompson, A.B., 1984. Pressure–temperature–time paths of regional metamorphism I. Heat transfer during the evolution of regions of thickened continental crust. *Journal of Petrology*, **25,** 894–928.

Erkan, K. & Blackwell, D.D., 2008. A thermal test of the post-subduction tectonic evolution along the California transform margin. *Geophysical Research Letters*, **35,** L07309.

Ernst, W.G., Hacker, B.R. & Liou, J.G., 2007. Petrotectonics of ultrahigh-pressure crustal and upper-mantle rocks – implications for Phanerozoic collisional orogens. In: *Whence the Mountains? Inquiries into the Evolution of Orogenic Systems: A Volume in Honor of Raymond A. Price*, Vol. 433 (eds Sears, J.W., Harms, T.A. & Evenchick, C.A.), pp. 27–49. The Geological Society of America Special Paper.

Ferriss, E.D.A., Essene, E.J. & Becker, U., 2008. Computational study of the effect of pressure on the Ti-in-zircon geothermometer. *European Journal of Mineralogy*, **20,** 745–755.

Ferry, J.M. & Watson, E.B., 2007. New thermodynamic models and revised calibrations for the Ti-in-zircon and Zr-in-rutile thermometers. *Contributions to Mineralogy and Petrology*, **154,** 429–437, doi:10.1007/s00410-007-0201-0.

Fraser, J.E., Searle, M.P., Parrish, R.R. & Noble, S.R., 2001. Chronology of deformation, metamorphism, and magmatism in the southern Karakoram Mountains. *Geological Society of America Bulletin*, **113,** 1443–1455.

Fuhrman, M.L. & Lindsley, D.H., 1988. Ternary-feldspar modeling and thermometry. *American Mineralogist*, **73,** 201–215.

Ganguly, J., Cheng, W. & Chakraborty, S., 1998. Cation diffusion in aluminosilicate garnets; experimental determination in pyrope–almandine diffusion couples. *Contributions to Mineralogy and Petrology*, **131,** 171–180.

Garlick, G.D., MacGregor, I.D. & Vogel, D.E., 1971. Oxygen isotope ratios in eclogites from kimberlites. *Science*, **172,** 1025–1027.

Gerya, T.V. & Yuen, D.A., 2003. Rayleigh–Taylor instabilities from hydration and melting propel 'cold plumes' at subduction zones. *Earth and Planetary Science Letters*, **212,** 47–62.

Ghent, E.D., 1976. Plagioclase–garnet–Al_2SiO_5–quartz: a potential geobarometer–geothermometer. *American Mineralogist*, **61,** 710–714.

Green, E., Holland, T. & Powell, R., 2007. An order-disorder model for omphacitic pyroxenes in the system jadeite–diopside–hedenbergite–acmite, with applications to eclogitic rocks. *American Mineralogist*, **92,** 1181–1189.

Hacker, B.R., 2006. Pressures and temperatures of ultrahigh-pressure metamorphism: implications for UHP tectonics and H_2O in subducting slabs. *International Geology Review*, **48,** 1053–1066.

Hacker, B.R., Gnos, E., Ratschbacher, L. *et al*., 2000. Hot and dry deep crustal xenoliths from Tibet. *Science*, **287,** 2463–2466.

Hacker, B., Luffi, P., Lutkov, V. *et al*., 2005. Near-ultrahigh pressure processing of continental crust: Miocene crustal xenoliths from the Pamir. *Journal of Petrology*, **46,** 1661–1687.

Harrison, T.M. & Schmitt, A.K., 2007. High sensitivity mapping of Ti distributions in Hadean zircons. *Earth and Planetary Science Letters*, **261,** 9–19.

Harrison, T.M., McKeegan, K.D. & Le Fort, P., 1995. Detection of inherited monazite in the Manaslu leucogranite by $^{208}Pb/^{232}Th$ ion microprobe dating: crystallization age and tectonic significance. *Earth and Planetary Science Letters*, **133,** 271–282.

Hetenyi, G., Cattin, R., Brunet, F. *et al*., 2007. Density distribution of the India plate beneath the Tibetan plateau: geophysical and petrological constraints on the kinetics of lower-crustal eclogitization. *Earth and Planetary Science Letters*, **264,** 226–244, doi: 10.1016/j.epsl.2007.09.036.

Hildebrand, P.R., Noble, S.R., Searle, M.P., Parrish, R.R. & Shakirullah, 1998. Tectonic significance of 24 Ma crustal melting in the eastern Hindu Kush, Pakistan. *Geology*, **26,** 871–874.

Hildebrand, P.R., Noble, S.R., Searle, M.P., Waters, D.J. & Parrish, R.R., 2001. Old origin for an active mountain range: geology and geochronology of the eastern Hindu Kush, Pakistan. *Geological Society of America Bulletin*, **113,** 625–639.

Hodges, K.H., 2000. Tectonics of the Himalaya and southern Tibet from two perspectives. *Geological Society of America Bulletin*, **112,** 324–350.

Hoering, T.C., 1961. The effect of physical changes on isotopic fractionation. *Carnegie Institute, Washington Yearbook*, **61,** 201–204.

Holdaway, M.J. & Lee, S.M., 1977. Fe-Mg cordierite stability in high grade pelitic rocks based on experimental, theoretical, and natural observations. *Contributions to Mineralogy and Petrology*, **63,** 175–198.

Holland, T.J.B. & Powell, R., 1998. An internally-consistent thermodynamic dataset for phases of petrological interest. *Journal of Metamorphic Geology*, **16,** 309–344.

Huberty, J.M., Kita, N.T., Kozdon, R. *et al*., 2010. Crystal orientation effects in $\delta^{18}O$ for magnetite and hematite by SIMS. *Chemical Geology*, **276,** 269–283.

Huerta, A.D., Royden, L.H. & Hodges, K.P., 1998. The thermal structure of collisional orogens as a response to accretion, erosion, and radiogenic heating. *Journal of Geophysical Research*, **103,** 15,287–15,302.

Hyndman, R.D., 2010. The consequences of Canadian Cordillera thermal regime in recent tectonics and elevation: a review. *Canadian Journal of Earth Sciences*, **47,** 621–632.

Jacob, D., Jagoutz, E., Lowry, D., Mattey, D. & Kudrjavtseva, G., 1994. Diamondiferous eclogites from Siberia: remnants of Archean oceanic crust. *Geochimica Cosmochimica Acta*, **58,** 5191–5207.

Johnson, M.R.W., 2002. Shortening budgets and the role of continental subduction during the India-Asia collision. *Earth Science Reviews*, **59,** 101–123.

Johnson, D.M., Hooper, P.R. & Conrey, R.M., 1999. XRF analysis of rocks and minerals for major and race elements on a single low dilution Li-tetraborate fused bead. *Advances in X-ray Analysis*, **41,** 843–867.

Keller, L.M., De Capitani, C. & Abart, R., 2005. A quaternary solution model for white micas based on natural coexisting phengite–paragonite pairs. *Journal of Petrology*, **46,** 2129–2144.

Kelly, J.L., Fu, B., Kita, N.T. & Valley, J.W., 2007. Optically continuous silcrete cements of the St. Peter sandstone: oxygen isotope analysis by ion microprobe and laser fluorination. *Geochimica Cosmochimica Acta*, **71,** 3812–3832.

Keppie, D.F., Currie, C.A. & Warren, C., 2009. Subduction erosion modes: comparing finite element numerical models with the geological record. *Earth and Planetary Science Letters*, **287,** 241–254.

Kita, N.T., Ushikubo, T., Fu, B. & Valley, J.W., 2009. High precision SIMS oxygen isotope analyses and the effect of sample topography. *Chemical Geology*, **264,** 43–57, doi:10.1016/j.chemgeo.2009.02.012.

Kita, N.T., Huberty, J.M., Kozdon, R., Beard, B.L. & Valley, J.W., 2011. High-precision SIMS oxygen, sulfur, and iron stable isotope analyses of geological materials: accuracy, surface topography and crystal orientation. *Surface and Interface Analysis*, **43,** 427–431, doi: 10.1002/sia.3424.

Krogh Ravna, E. & Paquin, J., 2003. Thermobarometric methodologies applicable to eclogites and garnet ultrabasites. In: *Ultrahigh-Pressure Metamorphism* (eds Carswell, D.A. & Compagnoni, R.), pp. 229–259. *European Union Notes in Mineralogy*, **5,** Budapest, European Union.

Krogh Ravna, E.J. & Terry, M.P., 2004. Geothermobarometry of phengite–kyanite–quartz/coesite eclogites. *Journal of Metamorphic Geology*, **22,** 579–592, doi:10.1111/j.1525-1314.2004.00534.x.

Lee, J., Hacker, B.R. & Wang, Y., 2004. Evolution of North Himalayan Gneiss Domes: structural and metamorphic studies in Mabja Dome, southern Tibet. *Journal of Structural Geology*, **26,** 2297–2316.

LePichon, X., Henry, P. & Goffé, B., 1997. Uplift of Tibet: from eclogites to granulites – implications for the Andean Plateau and the Variscan belt. *Tectonophysics*, **273,** 57–76.

Ludwig, K.R., 2003. *Isoplot/*Ex, 3.00. Berkeley Geochronology Center Special Publication, Berkeley, **4**, 70 pp.

Lutkov, V.S., 2003. Petrochemical evolution and genesis of potassium pyroxenite–eclogite–granulite association in the mantle and crustal xenoliths from Neogene fergusites of South Pamir, Tajikistan. *Geochimica Cosmochimica Acta*, **3,** 254–265.

McGraw, J., 2010. *Exhumation Depths of the Lower Crustal Domes of the Pamir*. MS Thesis, University of California, Santa Barbara, USA.

McGraw, J., Hacker, B.R., Ratschbacher, L. & Stübner, K., 2010. The high-grade crustal domes of the Pamir. In: *Proceedings for the 25th Himalaya–Karakoram–Tibet Workshop* (eds Leech, M.L. *et al*.), 1 pp. US Geological Survey, Santa Barbara, Open-File Report 2010–1099.

McKenzie, D. & Priestley, K., 2008. The influence of lithospheric thickness variations on continental evolution. *Lithos*, **102,** 1–11.

Mechie, J., Yuan, X., Schurr, B. *et al*., 2011. Project TIPAGE wide-angle seismic data reveals the crustal structure along a profile across the Pamir and southern Tien Shan. *Geophysical Research Abstracts*, **13,** EGU2011-2497.

Meyer, B., Tapponnier, P., Bourjot, L. *et al*., 1998. Crustal thickening in Gansu-Qinghai, lithospheric mantle subduction, and oblique, strike-slip controlled growth of the Tibet plateau. *Geophysical Journal International*, **135,** 1–47.

Meyre, C., DeCapitani, C. & Partzsch, J.H., 1997. A ternary solid-solution model for omphacite and its application to geothermobarometry of eclogites from the Middle Adula nappe (Central Alps, Switzerland). *Journal of Metamorphic Geology*, **15,** 687–700.

Milke, R., Wiedenbeck, M. & Heinrich, W., 2001. Grain-boundary diffusion of Si, Mg, and O in enstatite reaction rims: a SIMS study using isotopically doped reactants. *Contributions to Mineralogy and Petrology*, **142,** 15–26.

Mohadjer, S., Bendick, R., Ischuk, A. *et al*., 2010. Partitioning of India-Eurasia convergence in the Pamir-Hindu Kush from GPS measurements. *Geophysical Research Letters*, **37,** L04305.

Montel, J.M. & Vielzeuf, D., 1997. Partial melting of metagreywackes; part II, compositions of minerals and melts. *Contributions to Mineralogy and Petrology*, **128,** 176–196.

Nakamura, D. & Banno, S., 1997. Thermodynamic modeling of sodic pyroxene solid-solution and its application in a eclogite-facies–kyanite–coesite geothermobarometer for UHP metamorphic rocks. *Contributions to Mineralogy and Petrology*, **130,** 93–102, doi: 10.1007/s004100050352.

Nakamura, D. & Hirajima, T., 2005. Experimental evaluation of garnet-clinopyroxene geothermometry as applied to eclogites. *Contributions to Mineralogy and Petrology*, **150,** 581–588.

Negredo, A., Replumaz, A., Villaseñor, A. & Guillot, S., 2007. Modeling the evolution of continental subduction processes in the Pamir–Hindu Kush region. *Earth and Planetary Science Letters*, **259,** 212–225.

Nickel, K.G. & Green, D.H., 1985. Empirical geothermobarometry for garnet peridotites and implications for the nature of the lithosphere, kimberlites and diamonds. *Earth and Planetary Science Letters*, **73,** 158–170.

Nimis, P. & Grütter, H., 2010. Internally consistent geothermometers for garnet peridotites and pyroxenite. *Contributions to Mineralogy and Petrology*, **159,** 411–427.

Oxburgh, E.R. & Turcotte, D.L., 1974. Membrane tectonics and the East African rift. *Earth and Planetary Science Letters*, **22,** 133–140.

Page, F.Z., Ushikubo, T., Kita, N.T., Riciputi, L.R. & Valley, J.W., 2007a. High precision oxygen isotope analysis of picogram samples reveals 2-μm gradients and slow diffusion in zircon. *American Mineralogist*, **92,** 1772–1775.

Page, F.Z., Fu, B., Kita, N.T. *et al*., 2007b. Zircons from kimberlites: new insights from oxygen isotopes, trace elements, and Ti in zircon thermometry. *Geochimica Cosmochimica Acta*, **71,** 3887–3903.

Page, F.Z., Kita, N.T. & Valley, J.W., 2010. Ion microprobe analysis of oxygen isotopes in garnets of complex chemistry. *Chemical Geology*, **270,** 9–19.

Parrish, R.R. & Tirrul, R., 1989. U-Pb age of the Baltoro granite, northwest Himalaya, and implications for monazite U-Pb systematics. *Geology*, **17,** 1076–1079.

Patiño Douce, A.E., 2005. Vapor-absent melting of tonalite at 15–32 kbar. *Journal of Petrology*, **46,** 275–290.

Patiño Douce, A.E. & Harris, N., 1998. Experimental constraints on Himalayan anatexis. *Journal of Petrology*, **39,** 689–710.

Patiño Douce, A.E. & McCarthy, T.C., 1998. Melting of crustal rocks during continental collision and subduction. In: *When Continents Collide: Geodynamics and Geochemistry of Ultrahigh-Pressure Rocks* (eds Hacker, B.R. & Liou, J.G.), pp. 27–55. Kluwer Academic, New York.

Peacock, S.M., 1995. Ultrahigh-pressure metamorphic rocks and the thermal evolution of continent collision belts. *The Island Arc*, **4,** 376–383.

Pegler, G. & Das, S., 1998. An enhanced image of the Pamir–Hindu Kush seismic zone from relocated earthquake hypocenters. *Geophysical Journal International*, **134,** 573–595.

Perchuk, L.L. & Lavrent'eva, I.V., 1983. Experimental investigation of exchange equilibria in the system cordierite–garnet–biotite. In: *Kinetics and Equilibrium in Mineral Reactions, Advances in Physical Geochemistry*, Vol. 3 (ed. Saxena, S.K.), pp. 199–239. Springer, New York.

Pope, D.C. & Willett, S.D., 1998. A thermal-mechanical model for crustal thickening in the central Andes driven by ablative subduction. *Geology*, **26,** 511–514.

Proyer, A., Dachs, E. & McCammon, C., 2004. Pitfalls in geothermobarometry of eclogites: Fe3+ and changes in the mineral chemistry of omphacite at ultrahigh pressures. *Con-*

tributions to Mineralogy and Petrology, **147,** 305–318, doi: 10.1007/s00410-004-0554-6.

Ravna, E.J.K., 2000. The garnet-clinopyroxene Fe^{2+}-Mg geothermometer: an updated calibration. *Journal of Metamorphic Geology*, **18,** 211–219.

Reigber, C.H., Michel, G.W., Galas, R. *et al.*, 2001. New space geodetic constraints on the distribution of deformation in Central Asia. *Earth and Planetary Science Letters*, **191,** 157–165.

Renne, P.R., Mundil, R., Balco, G., Min, K. & Ludwig, K.R., 2010. Joint determination of 40K decay constants and 40Ar*/40K for the Fish Canyon sanidine standard, and improved accuracy for 40Ar/39Ar geochronology. *Geochimica et Cosmochimica Acta*, **74,** 5349–5367.

Robinson, A.C., Yin, A., Manning, C.E., Harrison, T.M., Zhang, S.-H. and Wang, X.F., 2007. Cenozoic evolution of the eastern Pamir: implications for strain-accommodation mechanisms at the western end of the Himalayan-Tibetan orogen. *Geological Society Of America Bulletin*, **119,** 882–896.

Root, D.B., Hacker, B.R., Gans, P.B., Ducea, M.N., Eide, E.A. & Mosenfelder, J.L., 2005. Discrete ultrahigh-pressure domains in the Western Gneiss Region, Norway: implications for formation and exhumation. *Journal of Metamorphic Geology*, **23,** 45–61.

Royden, L.H., 1993. The steady state thermal structure of eroding orogenic belts and accretionary prisms. *Journal of Geophysical Research*, **98,** 4487–4507.

Rumble, D. & Yui, T.-F., 1998. The Qinglongshan oxygen and hydrogen isotope anomaly near Donghai in Jiangsu Province, China. *Geochimica et Cosmochimica Acta*, **62,** 3307–3321.

Schmidt, M.W., Vielzeuf, D. & Auzanneau, E., 2004. Melting and dissolution of subducting crust at high pressures: the key role of white mica. *Earth and Planetary Science Letters*, **228,** 65–84.

Schuhmacher, M., de Chambost, E., McKeegan, K.D., Harrison, T.M. & Migeon, H., 1994. Dating of zircon with the CAMECA IMS 1270. In: *Secondary Ion Mass Spectrometry SIMS IX* (eds Benninghoven, A., Nihei, Y., Shimizu, R. & Werner, H.W.), pp. 912–922. Wiley, New York.

Schulze, D.J., Harte, B., Valley, J.W., Brenan, J.M. & Channer, D.M., 2003a. Extreme crustal oxygen isotope signatures preserved in coesite in diamond. *Nature*, **423,** 68–70.

Schulze, D.J., Valley, J.W., Spicuzza, M.J. & Channer, D.M.D., 2003b. Oxygen isotope composition of eclogitic and peridotitic garnet xenocrysts from the La Ceniza kimberlite, Guaniamo, Venezuela. *International Geology Review*, **45,** 968–975.

Schwab, M., Ratschbacher, L., Siebel, W. *et al.*, 2004. Assemblage of the Pamirs: age and origin of magmatic belts from the southern Tien Shan to the southern Pamirs and their relation to Tibet. *Tectonics*, **23,** TC4002, doi: 10.1029/2003TC001583.

Sharp, Z.D., 1995. Oxygen isotope geochemistry of the Al_2SiO_5 polymorphs. *American Journal of Science*, **295,** 1058–1076.

Sharp, Z.D., Essene, E.J. & Smyth, J.R., 1992. Ultra-high temperatures from oxygen isotope thermometry of a coesite-sanidine grospydite. *Contributions to Mineralogy and Petrology*, **112,** 358–370.

Sharp, Z.D., Essene, E.J. & Hunziker, J.C., 1993. Stable-isotope geochemistry and phase equilibria of coesite-bearing whiteschists, Dora Maira Massif, western Alps. *Contributions to Mineralogy to Petrology*, **114,** 1–12.

Spera, F.J., 1984. Carbon dioxide in petrogenesis III: role of volatiles in the ascent of alkaline magmas with special reference to xenolith-bearing mafic lavas. *Contributions to Mineralogy and Petrology*, **88,** 217–232.

Stearns, M., Hacker, B.R. & Kylander-Clark, A.R.C., 2011. Titanite geochronology from the mid to lower crust of the Pamir plateau, eastern Tajikistan. *Journal of Himalayan Earth Sciences*, **44,** 80.

Stípská, P. & Powell, R., 2005. Constraining the *P-T* path of a MORB-type eclogite using pseudosections, garnet zoning and garnet–clinopyroxene thermometry: an example from the Bohemian Massif. *Journal of Metamorphic Geology*, **23,** 725–743.

Strecker, M.R., Frisch, W., Hamburger, M.W. *et al.*, 1995. Quaternary deformation in the Eastern Pamirs, Tadjikistan and Kyrgyzstan. *Tectonics*, **14,** 1061–1079.

Taylor, W.R., 1998. An experimental test of some geothermometer and geobarometer formulations for upper mantle peridotites with application to the thermobarometry of fertile lherzolite and garnet websterite. *Neues Jahrbuch für Mineralogie – Abhandlungen*, **172,** 381–408.

Trail, D., Bindeman, I.N., Watson, E.B. & Schmitt, A.K., 2009. Experimental calibration of oxygen isotope fractionation between quartz and zircon. *Geochimica Cosmochimica Acta*, **73,** 7110–7126.

Valley, J.W., 2001. Stable isotope thermometry at high temperatures. In: *Stable Isotope Geochemistry* (eds Valley, J.W. & Cole, D.R.), *Reviews in Mineralogy and Geochemistry*, **43,** 365–414.

Valley, J.W., 2003. Oxygen isotopes in zircon. In: *Zircon* (eds Hanchar, J.M. & Hoskin, P.W.O.), *Reviews in Mineralogy and Petrology*, **53,** 343–385.

Valley, J.W. & Kita, N.T., 2009. *In situ* oxygen-isotope chemistry by ion microprobe. In: *MAC Short Course: Secondary Ion Mass Spectrometry in the Earth Sciences*, Vol. 91 (ed. Fayek, M.), pp. 19–63. Mineralogical Association of Canada, Toronto.

Valley, J.W., Kitchen, N., Kohn, M.J., Niendorf, C.R. & Spicuzza, M.J., 1995. UWG-2, a garnet standard for oxygen-isotope ratios: strategies for high precision and accuracy by laser heating. *Geochimica Cosmochimica Acta*, **59,** 5523–5531.

Valley, J.W., Bindeman, I.N. & Peck, W.H., 2003. Empirical calibration of oxygen isotope fractionation in zircon. *Geochimica Cosmochimica Acta*, **67,** 3257–3266.

Vielzeuf, D. & Holloway, J.R., 1988. Experimental determination of the fluid-absent melting relations in the pelitic system: consequences for crustal differentiation. *Contributions to Mineralogy and Petrology*, **98,** 257–276.

Vielzeuf, D. & Montel, J.M., 1994. Partial melting of metagreywackes; part 1, fluid-absent experiments and phase relationships. *Contributions to Mineralogy and Petrology*, **117,** 375–393.

Vlasov, N.G., Dyakov, Y.A. & Cherev, E.S., 1991. *Geological map of the Tajik SSR and adjacent territories, 1:500,000. Vsesojuznoi Geological Institute*. Saint Petersburg, Leningrad.

White, R.W., Powell, R. & Holland, T.J.B., 2007. Progress relating to calculation of partial melting equilibria for metapelites. *Journal of Metamorphic Geology*, **25,** 511–527.

Whitney, D.L. & Evans, B.W., 2010. Abbreviations for names of rock-forming minerals. *American Mineralogist*, **95,** 185–187.

Wolfsberg, M., 1972. Theoretical evaluation of experimentally observed isotope effects. *Accounts of Chemical Research*, **5,** 225–233.

Yund, R.A., 1997. Rates of grain boundary diffusion through enstatite and forsterite reaction rims. *Contributions to Mineralogy and Petrology*, **126,** 224–236.

Zheng, Y.-F., 1993a. Calculation of oxygen isotope fractionation in anhydrous silicate minerals. *Geochimica Cosmochimica Acta*, **57,** 1079–1091.

Zheng, Y.-F., 1993b. Calculation of oxygen isotope fractionation in hydroxyl-bearing silicates. *Earth and Planetary Science Letters*, **120,** 247–263.

Zheng, Y.-F., Fu, B., Li, Y., Xiao, Y. & Li, S., 1998. Oxygen and hydrogen isotope geochemistry of ultrahigh-pressure eclogites from the Dabie Mountains and the Sulu terrane. *Earth and Planetary Science Letters*, **155,** 113–129.

SUPPORTING INFORMATION

Additional Supporting Information may be found in the online version of this article:

Figure S1. Pseudosection for eclogite DK84. Excess SiO_2 was added to the bulk composition (Table 1) in order to suppress corundum at high pressure. Corundum is not found in the mineral assemblage. Multiple composition garnet rims were found within a single thin section of DK84; garnet isopleths are drawn for the garnet rim composition $Alm_{47}Prp_{25}Grs_{27}Sps_{01}$. Coe = coesite; Cpx = clinopyroxene; Fsp = feldspar; Grt = garnet; Ky = kyanite; Ol = olivine; Opx = orthopyroxene; Qz = quartz.

Figure S2. Pseudosection for garnet–omphacite granulite DK32, calculated using Perple_X. Coe = coesite; Cpx = clinopyroxene; Fsp = feldspar; Grt = garnet; Ky = kyanite; Ol = olivine; Opx = orthopyroxene; Qz = quartz.

Table S1. Electron microprobe mineral compositions from the Pamir Mountains xenoliths.

Table S2. Individual WiscSIMS ion-microprobe oxygen-isotope spot analyses of unknowns and standards.

Table S3. SHRIMP U–Pb zircon depth-profiling isotopic data.

Appendix S1. Analytical methods used in this study.

Appendix S2. Uncertainties associated with oxygen-isotope thermometry using the quartz–garnet, quartz–kyanite and quartz–zircon pairs.

Received 18 March 2011; revision accepted 4 January 2012.